



(*Thesis dissertation for partial fulfillment of M.Sc. degree*)

Performance Study of a Highly Efficient FeS₂ Based Thin-Film Solar Cell Using CuBi₂O₄ as a Back Surface Field Layer

Submitted by

MD. SHAH KAMAL

Exam Roll No.: 70406

Registration No.: 2013-012-407

Session: 2019-2020

**Department of Electrical and Electronic Engineering
Faculty of Engineering and Technology
University of Dhaka**

June 2022

Declaration

I, hereby, declare that the work presented in this thesis is the outcome of the investigation performed and authentically prepared by us under the supervision of **DR. MD. Habibur Rahman**, Professor, Department of Electrical and Electronic Engineering, University of Dhaka. To the best of our knowledge, it contains no materials which are exactly same which were previously published anywhere in print or soft.

MD. SHAH KAMAL

Exam Roll: 70406; Registration No: 2013-012-407

Year: M.Sc. (3rd Semester); Session: 2019-2020

Department of Electrical and Electronic Engineering,
University of Dhaka

Certificate

This is to certify that the M.Sc. 3rd semester thesis on "***Performance Study of a Highly Efficient FeS₂ Based Thin-Film Solar Cell Using CuBi₂O₄ as a Back Surface Field Layer***" has been submitted for the partial fulfillment of the degree of M.Sc. (Eng.) in Electrical and Electronic Engineering from the University of Dhaka, carried out by **MD. SHAH KAMAL**, under my supervision. According to my knowledge and as per declaration, the whole work and project report has been prepared by the student and has not been submitted anywhere else to any degree. The project report can be considered for evaluation. He is permitted to submit the project report.

DR. MD. HABIBUR RAHMAN

Professor

Department of Electrical and Electronic Engineering,
University of Dhaka.

Abstract

Thin film solar cells (TFSC) using semiconductor absorber layer such as CdTe, GaAs, CIGS, CZTS and others have emerged as the most attractive materials for photovoltaic technology for their excellent efficiency and compatibility with the fabrication process. But the traditional absorber materials in TFSCs still face issues such as scarcity of resources, high costs of materials processing and device fabrication stages which restrict the use of solar energy in a broad scale. Recently Iron pyrite (FeS_2) thin film has recently piqued the scientific community's interest for its optimum band gap (0.95 eV), low manufacturing cost, non-toxicity and very high absorption coefficient ($> 10^5 \text{ cm}^{-1}$ for $h\nu > 1.3\text{-}1.4 \text{ eV}$) with excellent minority carrier diffusion length. In this project, we have proposed a highly efficient FeS_2 based thin film solar cell incorporating with GaAs as a buffer layer and CuBi_2O_4 as the back surface field (BSF) layer. A well-known popular simulator, SCAPS 1D is used to simulate the numerical analysis of the suggested structure. The physical characteristics used in the investigation were taken from the different literatures. The effects of FeS_2 and CuBi_2O_4 layer thickness, doping and defect concentration on the performance of the solar cell has been thoroughly investigated. With $J_{\text{SC}} = 46.34 \text{ mA/cm}^2$, $V_{\text{OC}} = 0.517 \text{ V}$, and $\text{FF} = 80.02 \%$, the power conversion efficiency (PCE) of the n-GaAs/p- FeS_2 based solar cell is 19.1881%, where with the addition of a CuBi_2O_4 as back surface field (BSF) layer, the solar cell's PCE increases up to 34.7 % with $J_{\text{SC}} = 49.64 \text{ mA/cm}^2$, $V_{\text{OC}} = 0.8426 \text{ V}$, and $\text{FF} = 79.58\%$ respectively. This gain in efficiency is mostly due to the increase of open circuit voltage, V_{OC} which is a result of the dual-heterojunction suitable band alignment. These findings show that a FeS_2 based thin film solar cell with GaAs and CuBi_2O_4 layer could be a potential option for producing high-efficiency thin film solar cells technology for future solar energy harvesting.

Table of Contents

Declaration.....	i
Certificate.....	ii
Abstract.....	iii
Table of Contents.....	iv
List of Figures.....	vi
List of Tables.....	vii
Acronyms.....	vii
Chapter Introduction.....	1
1.1 Global Energy Challenges.....	1
1.2 Renewable Energy: Future of Energy.....	2
1.3 Applications of Solar Energy.....	3
1.4 A Brief History of Solar Cell.....	4
1.5 FeS ₂ Based Solar Cell.....	5
1.6 Objectives and Goals.....	7
1.7 Outline of the Project.....	8
Chapter 2 Theory of Solar Cell.....	9
2.1 PV Effect.....	9
2.2 PN Junction.....	10
2.3 Solar Cell Parameters.....	13
2.4 Equivalent Circuit of Solar Cell.....	15
2.5 Air Mass.....	15
2.6 Solar Spectrum.....	16
2.7 Restrictions and Losses.....	17
2.8 Evolution of Solar Cell.....	18
2.9 Thin Film Solar Cells Technology.....	20
Chapter 3 Literature Review.....	22
3.1 Properties of the Materials.....	22
3.2 FeS ₂ Based Solar Cell Technology.....	25
3.3 CuBi ₂ O ₄ Based Solar Cell Technology.....	27
3.4 GaAs Based Solar Cell Technology.....	28
Chapter 4 Material & Methodology.....	29
4.1 SCAPS-1D.....	29
4.2 Device Modeling.....	33
4.3 Design Parameters.....	35
Chapter 5 Results & Discussion.....	37
5.1 Structure Analysis.....	37

5.2 Optimization of Proposed Structure.....	40
5.3 The Effects of Series and Shunt Resistance.....	46
5.4 The Effects of Temperature.....	48
5.5 Optimized Cell Performances of Fes2 Based Structure.....	49
Chapter 6 Conclusion & Future Works.....	51
6.1 Conclusion.....	51
6.2 Future Works.....	51
References.....	53

List of Figures

1.1 Change of Electricity Price from Various Sources.....	2
1.2 Growth of Renewable Energy.....	3
1.3 Price trend of solar cell.....	7
2.1 Photovoltaic Effect.....	10
2.2 The graphical solution to Poisson's equation for an abrupt p-n junction....	11
2.3 J-V Characteristics of p-n junction with and without Illumination.....	13
2.4 The equivalent circuit of (a) an ideal solar cell; and (b) a solar cell with series resistance R_S and shunt resistance R_{SH}	15
2.5 Air Mass Determination.....	16
2.6 AM 1.5 Solar Spectrum.....	17
3.1 FeS ₂ Crystal Structure.....	22
3.2 CuBi ₂ O ₄ Crystal structure.....	23
3.3 GaAs Crystal Structure.....	24
3.4 Price Comparison of Various PV materials.....	26
4.1 Action Panel of SCAPS-1D.....	29
4.2 Layer Editing Panel.....	30
4.3 Contact Editing Panel.....	31
4.4 Defect Simulation Panel.....	32
4.5 Typical Structure of FeS ₂ Based Solar Cell.....	34
4.6 Proposed Structure of FeS ₂ /CuBi ₂ O ₄ Based Solar Cell.....	34
5.1 J-V characteristics curve of conventional and proposed structure.....	38
5.2 Generation rate of the later structure.....	38
5.3 Spectral response of typical and FeS ₂ /CuBi ₂ O ₄ absorber solar cell.....	39
5.4 Band diagram of FTO/GaAs/FeS ₂ /CuBi ₂ O ₄ structure.....	39
5.5 Effect on (a) J_{SC} , (b) V_{OC} , (c) FF and (d) η with the variation of Thickness of CuBi ₂ O ₄ for FeS ₂ layers.....	41
5.6 Effect on (a) J_{SC} , (b) V_{OC} , (c) FF and (d) η with the variation of Doping Concentration of CuBi ₂ O ₄ for FeS ₂ layers.....	43
5.7 Effect on (a) J_{SC} , (b) V_{OC} , (c) FF and (d) η with the variation of Doping Concentration of FeS ₂ for CuBi ₂ O ₄ layers.....	44
5.8 Effect on (a) J_{SC} , (b) V_{OC} , (c) FF and (d) η with the variation of Defect Level Density of CuBi ₂ O ₄ for FeS ₂ layers.....	46
5.9 Effect on (a) J_{SC} , (b) V_{OC} , (c) FF and (d) η with the variation of Series Resistance.....	47
5.10 Effect on (a) J_{SC} , (b) V_{OC} , (c) FF and (d) η with the variation of Shunt Resistance.....	48
5.11 Influence on (a) J_{SC} , (b) V_{OC} , (c) FF and (d) η with the variation of Temperature.....	49
5.12 J-V Characteristics for optimal structure.....	49

List of Tables

4.1 Parameters of n-GaAs/p-FeS ₂ /p+-CuBi ₂ O ₄ solar cell.....	35
4.2 Parameters of interfaces used in this simulation.....	36
4.3 Parameter for Contacts.....	36
5.1 Optimum thickness for proposed structure.....	42
5.2 Optimum Doping Profile for Proposed Structure.....	45
5.3 Device performance of the optimized FeS ₂ based solar cells.....	50
5.4 Performance of the proposed solar cell in comparison with other thin film solar cells.....	50

Acronyms

Symbol	Explanation
PCE	Power conversion efficiency
FF	Fill factor
Voc	Open circuit voltage
Jsc	Short circuit current density
J₀	Diode saturation current density
I	Diode current
I₀	Diode saturation current
V_D	Diode voltage
V_T	Thermal voltage
E	Photon energy
v	Frequency of light
c	Speed of light
λ	Wavelength
V	Applied potential
I_L	Light generated photon current
f_t	Probability of occupation of trap state
D	Diffusion constant
α	Absorption coefficient
G	Generation rate
k	Boltzmann constant
T	Temperature
Q	Charge
V_{th}	Thermal velocity of charge carriers
δ_p	Capture cross section area of hole
δ_n	Capture cross section area of electron
E_c	Conduction band minimum
E_v	Valence band minimum
E_{fn}	Electron quasi-Fermi level
E_{fp}	Hole quasi-Fermi level
ΔE_c	Conduction band offset
ΔE_v	Valence band offset
N_A	Uniform acceptor density
N_D	Shallow uniform donor density
τ_e	Electron lifetime
τ_h	Hole lifetime
L_n	Electron diffusion length
L_p	Hole diffusion length
CBO	Conduction band offset

<i>VBO</i>	Valance band offset
<i>R_{iF}</i>	Interface recombination
<i>S_{iF}</i>	Interface recombination velocity
<i>Si</i>	Silicon
<i>ZnO</i>	Zinc Oxide
<i>TiO₂</i>	Titanium dioxide
<i>ZnS</i>	Zinc sulfide
<i>CMO</i>	Calcium manganese oxide
<i>FTO</i>	Fluorine doped tin oxide
<i>ETL</i>	Electron transport layer
<i>HTL</i>	Hole transport layer

Symbol	Explanation	Unit
PCE	Power conversion efficiency	%
FF	Fill factor	%
V_{oc}	Open circuit voltage	V
J_{sc}	Short circuit current density	mA/cm ²
J_0	Diode saturation current	mA/cm ²
I	Diode current	A
I_0	Diode saturation current	A
V_D	Diode voltage	V
V_T	Thermal voltage	V
E	Photon energy	eV
ν	Frequency of light	hz
c	Speed of light	m/s
λ	Wavelength	nm
V	Applied potential	V
I_L	Light generated photon current	A
D	Diffusion constant	m ² /s
α	Absorption coefficient	cm ⁻¹
k	Boltzmann constant	m ² kgs ⁻² K ⁻¹
T	Temperature	K
Q	Charge	C
V_{th}	Thermal velocity of charge carriers	m/s
δ_p	Capture cross section area of hole	cm ²
δ_n	Capture cross section area of electron	cm ²
E_c	Conduction band minimum	eV
E_v	Valence band minimum	eV
E_{fn}	Electron quasi-Fermi level	eV
E_{fp}	Hole quasi-Fermi level	eV
ΔE_c	Conduction band offset	eV
ΔE_v	Valence band offset	eV
N_A	Uniform acceptor density	cm ⁻³
N_D	Shallow uniform donor density	cm ⁻³
τ_e	Electron lifetime	s
τ_h	Hole lifetime	s
L_n	Electron diffusion length	m
L_p	Hole diffusion length	m
CBO	Conduction band offset	eV
VBO	Valance band offset	eV
S_{if}	Interface recombination velocity	cm/s

Chapter 1

Introduction

1.1 Global Energy Challenges

The world will consume two-thirds more energy than it does now as the primary energy consumers by 2030. Globally oil, coal, and gas will remain the principal energy sources, according to the International Energy Agency (IEA) of Paris. Which is more than 90% of the predicted rise in demand during 2004. Natural gas will be the fastest increasing fuel, doubling in volume over the 2000–2030 projected period due to its relative abundance and environmental friendliness. Oil consumption will continue to climb with most of the growth in transportation sector. Renewable energy sources will contribute more to electricity generation in the future. However, wind and biomass will grow from a minimal base. Over the next few decades, the world's energy business will face four critical challenges. These include addressing global oil shortages, ensuring energy security, combatting environmental degradation, and satisfying the developing world's expanding requirements. However, somewhere within the first half of this century, a shift from fossil fuels to a non-carbon-based global economy will begin, significantly impacting the type of environment faced by future generations. While science may recommend the ideal time to initiate the shift, economic and political factors will play a more prominent role [1].

Every day we use about a million terajoules of energy, roughly equivalent to boiling 70 kettles of water for 7.5 billion people. Since the 1850s, humanity has sucked up almost 135 billion tons of crude oil to power cars, power plants, houses etc. The world's principal energy supply now comes from renewable resources like wind, solar, hydro and geothermal. This industry is expected to grow at a 2.6% annual rate until 2040. However, recent advances in solar panel technology have resulted in a large increase in the amount of energy generated by the sun [2,3].

World oil and gas reserves are dwindling fast. According to Kenneth Deffeyes' book, M. King Hubbert predicted in 1956 that US oil output would peak in the early 1970s. Hubbert's analysis was almost universally disregarded by the oil industry. Until 1970, when the US crude oil output began to fall. Experts began applying Hubbert's technique to world oil output from 1995, with most forecasting the peak year between 2004 and 2008. These studies were published in popular magazines including Nature, Science and Scientific American [4].

The 2008 global oil price peak of over \$140 per barrel seems to confirm these predictions. The US possesses proven oil and natural gas reserves which would last just 3.0 and 7.5 years respectively if the US depended solely on its reserves [5].

As a result of this "impending global oil shortfall," power costs are expected to rise dramatically over the next five to ten years. This impacts the economics of solar cell power, as solar modules based on semiconductor devices have a life expectancy of 25 years or more. Modern cost comparisons for solar cell electricity assume a short payback period and stable energy costs [6].

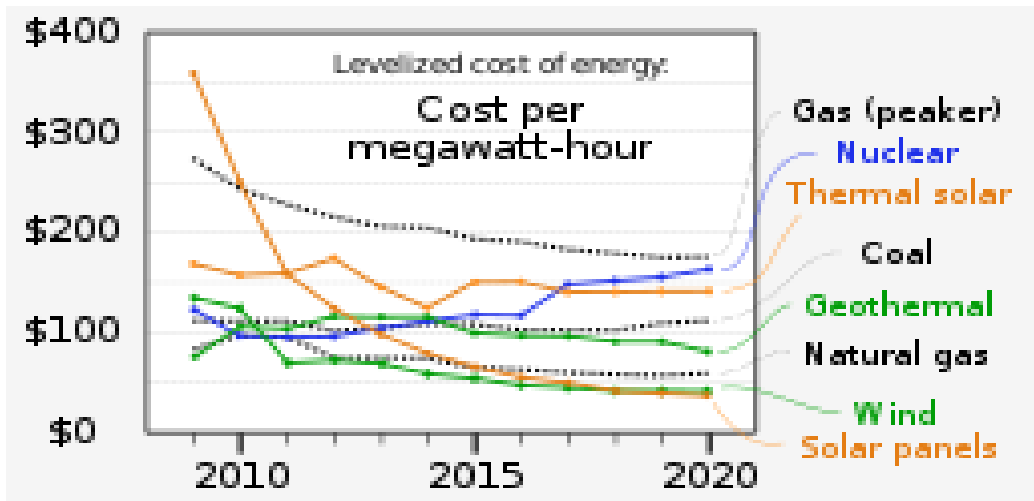


Figure 1.1: Change of Electricity Price from Various Sources [7].

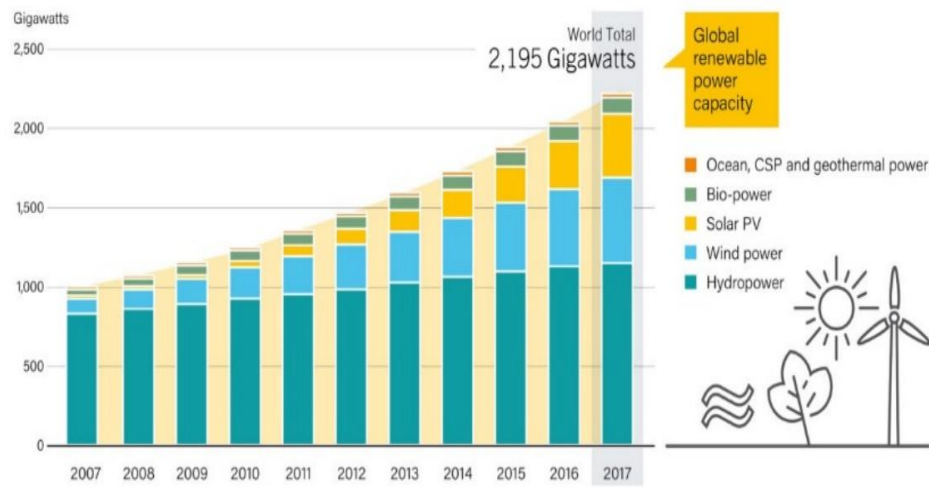
1.2 Renewable Energy: Future of Energy

Energy obtained from naturally regenerating but flow-limited sources is referred to as renewable energy. Renewable resources have a finite energy production per unit of time but have a nearly endless lifespan. Renewable energy is unlimited, clean, and more competitive. They vary from fossil fuels primarily in their diversity, availability, and global accessibility, but above all, they create neither greenhouse gases, which cause climate change, nor harmful emissions. The general cost trend is moving in the other way instead of a lower overall cost of fossil fuels. Half of all new power production capacity was built in 2014 with renewable energy is the second-largest source worldwide. According to the IEA, world electricity consumption will have climbed by 70% by 2040, and its proportion of final energy consumption will rise from 18% to 24% during the same timeframe. To address climate change, energy production must be clean. The second hottest year on record was 2019. National Geographic claims that the Earth's temperature has risen by 0.85°C since the end of the 19th century. Meanwhile over 1.1 billion people (17%) lack access to electricity. Two billion people (38%) utilize traditional biomass for cooking, heating, and lighting, endangering their health [8].

Renewable energy sources include the following:

- Wind energy is produced by using mechanical energy by wind flow.
- The main technologies employed here are solar photovoltaic and solar thermal.
- Rivers and other freshwater bodies create hydropower. Biomass and biogas: organic energy sources
- The heat in the Earth generates geothermal energy.
- Wave energy is the energy emitted by ocean waves.
- Bioethanol is an organic fuel suited for automobiles that is produced by the fermentation of plants. Biodiesel is an organic fuel derived from vegetable oils that is used in cars and other purposes.

Global Renewable Power Capacity, 2007-2017



REN21 RENEWABLES 2018 GLOBAL STATUS REPORT

Figure 1.2: Growth of Renewable Energy [9].

1.3 Applications of Solar Energy

Around 1990, solar cells were widely used to provide site-specific electricity for urban and suburban homes, businesses and other important grid-connected applications. Also, solar cell power systems have become important energy sources in poorer nations. Solar cell electricity is the cheapest and most efficient way to meet today's energy demands.

There are presently many types of photovoltaic (PV) systems being utilized on Earth including-

- Stand-alone remote systems with no battery storage.
- Standalone remotes with batteries
- Little calculator and toy modules
- Grid-connected DC to AC inverters for homes
- Commercial grid-connected inverter systems
- Utility-scale PV fields
- Self-contained solar cell power without batteries is remote solar water pumping.

Solar water pumping is a great solution for crop irrigation, livestock watering and rural town water supply. Globally solar water pumping devices are already in use. This application benefits from just pumping subsurface water when the sun shines. Instant agricultural irrigation is possible. In other areas, it is used to water cattle. With less disease, pumping subsurface water for human use in third-world countries is a good thing! The system's simplicity makes this application very cost-effective. No battery storage or DC to AC conversion is required. Simple solar trackers are used to speed up pumping. The electric motors that drive the pumps use current to run. By tracking the sun, this energy is available from dawn to dusk rather than just around midday. Air conditioning is another use where supply and demand are balanced in developed countries like the US. Various remote applications need to store electric energy till needed. Outposts and remote telecom repeater sites are two examples. Secondary or storage batteries are the best answer for most solar cell storage applications. Solar-powered calculators

are another well-known application. While amorphous silicon solar cells are less efficient than single or multi-crystalline cells, thin-film cells have the advantage of having built-in interconnectivity. Power calculators, for example amorphous silicon circuits are utilized to save the expense of combining several cells to generate voltage. The Japanese deserve credit for recognizing this benefit as do the creators of amorphous silicon solar cells [10,11].

1.4 A Brief History of Solar Cell

The solar cell's history is quite fascinating. Edmond Becquerel discovered in 1839 that when two distinct brass plates were submerged in a liquid and exposed by sunshine, they generated a continuous current. We now think that he created a thin-film copper-cuprous oxide solar cell. W. G. Adams and R. E. Day determined selenium possessed photovoltaic properties in the late 1870s. Amorphous selenium sheet mounted on metal backing covered with translucent gold leaf. When exposed to sunshine, the selenium array produced a current. There was no quantum theory back then, thus his claim of turning sunlight into electricity was questioned. So he sent a sample to Werner Siemens, one of the world's leading electrical experts. Siemens' observation backed with Fritts' claims. However, the efficiency of the thin-film cuprous oxide and amorphous selenium solar cells were less than 1%. Quantum physics was discovered some 75 years after single-crystal semiconductors were recognized as important [12].

In 1954, Chapin et al. [13] at Bell Labs discovered, built, and tested the 6% efficient silicon single-crystalline solar cell. Researchers improved silicon solar cell efficiency to 15% during the next four years. The time was appropriate as Sputnik was launched in 1957 and solar cells were the ideal remote electric power source due to their light weight and low maintenance. It now runs on silicon solar cells. After the 1973 Arab oil embargo, the solar cell industry grew. So far, low-volume yet reliable cell and array manufacture and performance had established the solar cell business. During the first two decades, dependability trumped cost. After 1973, the flat-plate silicon module was lowered to Earth and weather-proofed. This move also includes major cell and module manufacturing improvements that reduced costs. Flat plate "champion" silicon cells now have 25% efficiency. Production module efficiency has risen from around 10% in the early days to up to 19% currently (Sun Power Corporation). Above all, annual output levels have increased. Global output reached 1 gigatons in 2002 and 3.8 gigatons in 2006.

Using multi-crystalline wafers to manufacture good cells was discovered in the late 1970s [14]. Only carriers within an optical absorption length of the crystal boundaries are lost. This is less than 5% of carriers. Multicrystalline cells have an efficiency of around 14%, while identical single-crystalline cells have an efficiency of around 15%. By 2007, multi-crystalline modules sold roughly 45% of all modules, while single-crystalline modules sold around 40%. A huge learning curve enabled by single-crystal silicon and integrated circuit technological improvement led to planar silicon cell modules dominating the market in 2007. While silicon-based cells continue to dominate the solar energy market, other cell types have emerged in recent years. (Photovoltaic cells are also called solar cells.) These new cell types opened up new applications and low-cost solar energy production options. Alternate cell types include hydrogenated amorphous silicon, cadmium telluride and CIGS thin-film cells [15].

1.5 FeS₂ Based Solar Cell

Commercial solar cells are mostly crystalline in nature. But the production cost of these materials is relatively high compared to polycrystalline and monocrystalline combinations. Due to silicon's weak absorption coefficient, 200-500 nm thick absorber layers are used to absorb substantial amounts of sunlight. Due to weak absorption and high absorber layer area for silicon, the optimal absorber layer thickness is 5000 m [16,17].

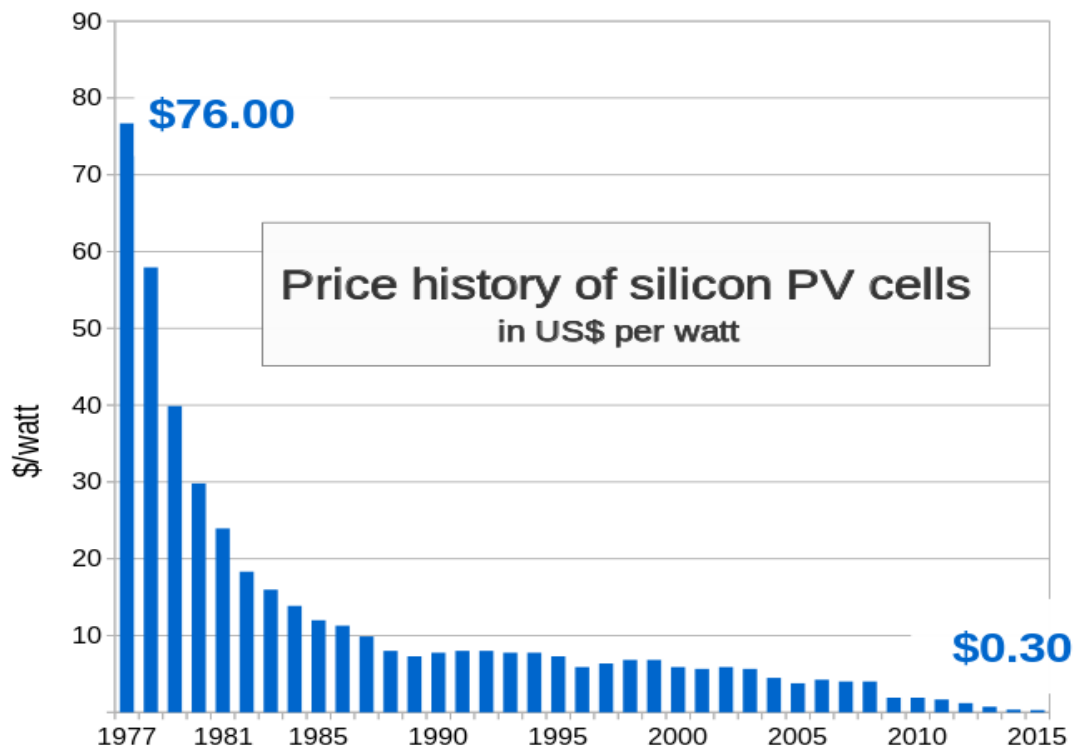
Thin film technology uses less material than silicon and has lower processing costs. Solar thin film technology is a prominent topic of research in industry since it is one of the most cost-effective and efficient ways to make solar cells. They are ideal for low- and high-volume solar cell applications. The demand for renewable energy sources is rising [18,19].

Solar energy is a free alternative energy source provided by nature. Photovoltaic (PV) systems are widely used because of the energy crisis and escalating energy demands. Importance of PV devices due to limited fossil fuel resources and associated carbon greenhouse impact. Increasing demand for low-cost PV devices with improved energy conversion efficiency pushes global research into smaller, cheaper materials and more efficient device architectures. To meet customer demand and generate electricity, high-power conversion efficiency solar cells with low material degradation are manufactured.

Thin film technologies like CdTe and CIGS cells have attained record efficiencies close to 20% [20,21]. Unfortunately, cadmium is poisonous and gallium, indium, and tellurium are scarce and costly. Those materials must be replaced if PV technology is to scale up to today's non-renewable energy production [22]. Quaternary blends are a good alternative absorber material because their PV properties can be tailored by varying the stoichiometry of individual components. Cu₂ZnSnS₄ (CZTS) has a 10% efficiency [23]. The materials are readily available, but tailoring their PV characteristics is a challenge.

Iron Pyrite is the most appealing choice for thin film PV applications (FeS₂). Iron pyrite is a common transition metal di-chalcogenide (TMD) with unique electronic and optical properties. As an example, it has a direct band gap of 1.05–1.10 eV which is equivalent to Si's (1.1 eV), but an indirect band gap of 0.95 eV. To Shockley-Queisser efficiency, FeS₂ solar cells could be nearly as efficient as Si solar cells. FeS₂ high absorption coefficient allows for the fabrication of a thin absorber layer of 20 nm or less, which other thin-film solar cell materials do not allow. It implies a significant reduction in the production cost (\$/W) of electricity. As a result, FeS₂ has received interest as a non-toxic super absorber material for thin-film solar cells [24,25].

In 1984, Ennaoui et al. Proposed and developed the FeS₂ solar cell. This sparked a huge rise in fes₂ based solar cell development in the years that followed. However, due to low solar energy conversion efficiency, this high desire became frustration (2.8%). This low efficiency was attributed to a photovoltage of 200 mv or 20% of its band gap. So, from 1984 until now, a lot of research has gone into figuring out the core cause of this unexpectedly low photovoltage. The primary explanations in the literature include surface inversion, deep donor state ionization, and photocarrier loss [26,27].



Source: Bloomberg New Energy Finance & pv.energytrend.com

Figure 1.3: Price trend of solar cell [24,25].

1.6 Objectives and Goals

The parameters of FeS_2 in this study, numerical modeling, is used to estimate or examine photovoltaic thin film solar cells. A noble material CuBi_2O_4 , was used as heterojunction bilayer absorber as well as a back surface field (BSF) to improve efficiency. In thin film solar cell technology, CuBi_2O_4 has emerged as a promising material [28]. The device modeling is done with the SCAPS 1D simulation software. To investigate the performance of a photovoltaic device, numerical analysis was performed on numerous physical aspects such as absorber thickness and doping concentration, buffer and window layers, temperature effect, and influence of solar illumination power on a solar cell. This research could aid in the development of thin-film solar cells with high conversion efficiency.

The following are the primary goals and objectives of the study reported in this report:

- Use SCAPS-1D for the numerical analysis of the proposed solar cell in one dimension.
- Analyze the performance metrics (open circuit voltage, short circuit current density, fill factor and efficiency)
- Determine the impact of a buffer layer on the performance of solar cells.
- Determine the impact of a BSF layer on the performance of solar cells.
- Propose a structure of a solar cell based on FeS_2 .

1.7 Outline of the Project

This report is divided into five sections, each of which is explained below.

- This project's first chapter (Chapter 1) has a brief introduction, problem statement, and objectives. It also explains how to organize a report.
- The principles of the solar cell and recombination losses in solar cells are covered in Chapter 2.
- The literature reviews of prior efforts are described in Chapter 3.
- Chapter 4 discusses technique and numerical analysis in SCAPS 1D.
- The findings of the simulation are described and discussed in Chapter 5.

Chapter 2

Theory of Solar Cell

2.1 PV Effect

The Photovoltaic (PV) is the process of converting electromagnetic radiation, such as light, into electrical energy is known as effect. [29]. However, the photoelectric and PV effects were not generally understood until Einstein articulated his theories on light [30]. According to quantum physics' wave-particle duality principles, light is made up of discrete energy quanta called photons, each having an energy (E) that depends on its wavelength (λ).

$$E = \frac{hc}{\lambda} \quad (2.1)$$

where h is Planck's constant and c is the speed of light. E is commonly given in unit eV, and λ in unit nm.

The energy gap between the outermost full electronic states at energy E_V and the following set of possible unoccupied states at energy E_C is represented in Figure 2.1. The valence band is made up of outer filled states populated by valence electrons that establish electronic bonds in the material. In the valence band, holes are quasiparticles with a $+q$ charge. The conduction band is the accessible vacant states above the gap. The conduction band electrons are delocalized and carry the charge $-q$. The bandgap is the energy gap between two bands (E_g). With more energy than E_g , photons absorbed in a semiconductor excite electrons, transporting them from the valence to conduction band, leaving holes behind, and thereby producing electron-hole pairs.

Normally, electron-hole couples recombine, releasing energy as light or heat. To use the electron-hole pair creation as electrical energy, the electron and hole must be separated before recombining. It is a potential difference that increases with successful separation. If an external load is connected, a current must flow across the circuit to make electrical work. The p-n junction is the most significant characteristic of a semiconductor solar cell because it separates electrons from holes. The p-n junction collects electrons that have been stimulated from the valence band to the conduction band. The current flows in the opposite direction to the electrons. Blue front layers and red absorber layers depict p-type layers. Section 2.2 discusses p- and n-type semiconductors, while Section 2.3 discusses Fermi level E_F . Adapted from [31].

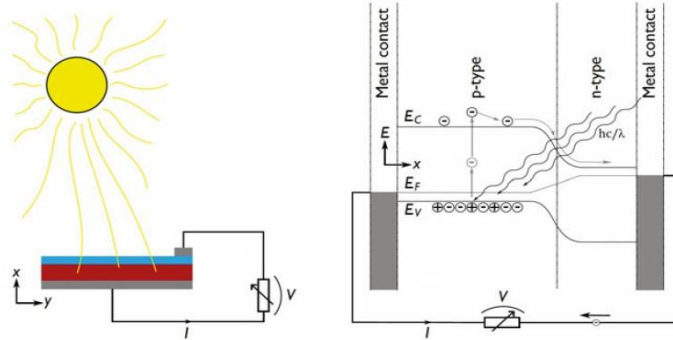


Figure 2.1: Photovoltaic Effect [31].

2.2 PN Junction

P type semiconductors are characterized by the presence of a hole majority charge carrier and are formed by defects that accept (N_A) electrons from the valence band, doping it with holes (p). Defects that donate (N_D) electrons (n) to the conduction band are used to achieve N-type doping. The p-n junction is formed when p-type and n-type semiconductors come into contact. Even though each semiconductor is electrically neutral, a diffusion process begins due to the variation in predominant charge carrier densities. Electrons diffuse into the p-type side to occupy the state previously held by a hole on the n-type side, and vice versa. As a charge carrier goes from one semiconductor type to another, the charge balance in the so-called space charge region (SCR), which becomes depleted of free charge carriers, changes. An electrical field flows from the n-type (now positively charged donor defects) semiconductor to the p-type semiconductor due to the changing charge balance in the SCR (negatively charged acceptor defects). Free charge carriers will be promoted (drifting) in one direction and opposed in the other, depending on their charge. As a result, the p-n junction will have two opposing forces: diffusion and drift. Electric current refers to moving charges, and the hole current density J_h and electron current density J_e each have a drift and diffusion component.

$$J_p = q(\mu_p \mathbf{p} \cdot \boldsymbol{\xi} - D_p \nabla \cdot \mathbf{p}) \quad (2.2)$$

$$J_n = q(\mu_n \mathbf{n} \cdot \boldsymbol{\xi} - D_n \nabla \cdot \mathbf{n}) \quad (2.3)$$

$J_{tot} = J_p + J_n$ is the overall current density. $J_{tot} = 0$ when everything is in balance. The electric field, mobility and carrier concentrations p and n all influence the drift current densities. The carrier concentration gradients and the diffusion constant are proportional to the diffusion current densities (D). The Nernst Einstein equation connects mobility and diffusion constant.

$$D = \frac{\mu k_B T}{q} \quad (2.4)$$

where, k_B is Boltzmann's constant and T is temperature. In the SCR, free charge carriers are in low concentration and will be swept away by the electrical field. The depletion width is W_D . We can use Poisson's electrostatic equation to calculate the total charge concentration, built-in electrical field $\boldsymbol{\xi}$ and potential ψ in a structure.

$$-\nabla^2 \psi = \nabla \cdot \boldsymbol{\xi} = \frac{\rho}{\epsilon} \quad (2.5)$$

Where ϵ is the dielectric permittivity. Figure 2.2 shows the solution of Poisson's equation in 1-D for a basic abrupt p-n junction. In a stable state, continuity (charge conservation) demands that

$$\nabla \cdot J = q(G - U) \quad (2.6)$$

where U is the net recombination rate and G is the net generation rate. The essential semiconductor physics equations (2.4), (2.5), and (2.6) provide the foundation for any solar cell device modeling.

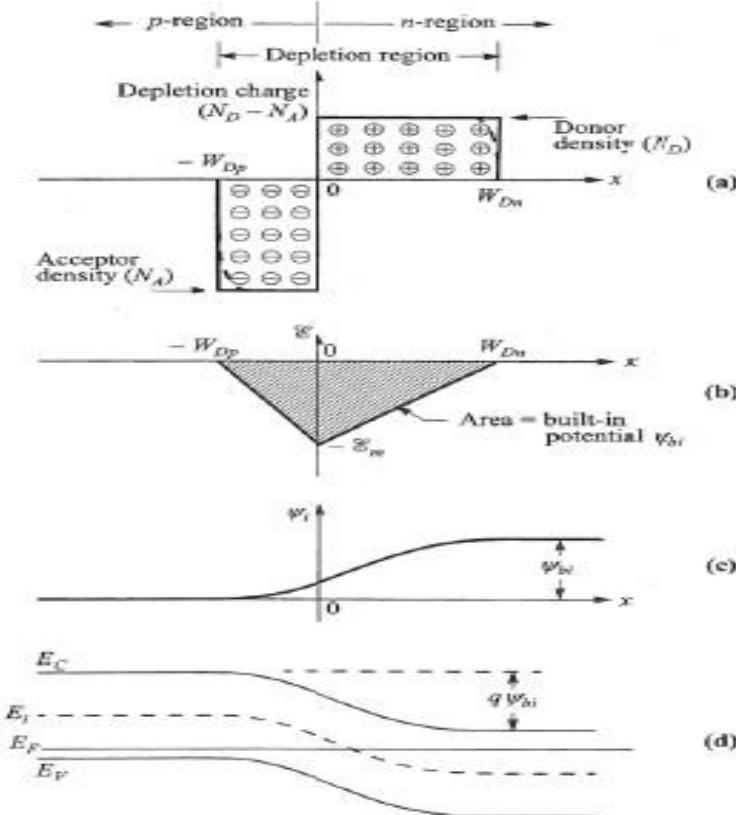


Figure 2.2: The graphical solution to Poisson's equation (2.5) for an abrupt p-n junction [32].

Using Fermi-Dirac statistics, the Fermi function describes the likelihood of finding a free charge carrier at energy E .

$$F(E) = \frac{1}{1 + \exp\left(\frac{E - E_F}{k_B T}\right)} \quad (2.7)$$

Where E_F is the Fermi level, defined as the energy at which a free carrier is 50% likely to be found. T is the temperature that determines the probability of curve's edge. Because thermal excitation of electrons from the valence band to the conduction band occurs at 0 K, the Fermi function becomes a step function. Thermal excitation is dependent on the semiconductor's density of states (DOS) for each energy band. Near the band's margins, where the action is, an effective DOS can be used to approximate the DOS.; N_V^* for the valence band and N_C^* for the conduction band. The free charge carriers are then

$$n = N_c^* \exp\left(\frac{(E_C - E_F)}{k_B T}\right) \quad (2.8)$$

$$p = N_V^* \exp \frac{(E_V - E_F)}{k_B T} \quad (2.8)$$

where E_V and E_C are the band edge energy of respective band. A defect-free intrinsic semiconductor will have a total concentration of electrons and holes such that $n = p$, and where $E_F = E_i \approx E_g/2$, if $N_V^* \approx N_C^*$. The intrinsic carrier concentration, in equilibrium conditions, is defined

$$\eta_i = \sqrt{np} \quad (2.9)$$

and consequently,

$$n_i^2 = N_V^* N_C^* \exp \left(-\frac{E_g}{k_B T} \right) \quad (2.10)$$

For a semiconductor with deliberate doping or intrinsic doping concentration defects $n \neq p$, but eq. (2.8) and (2.9) still apply. In this case, to maintain charge neutrality,

$$p + N_D^+ = n + N_A^- \quad (2.11)$$

But in non-equilibrium conditions, such a voltage bias or light illumination.

$$n_i^2 \neq np \quad (2.12)$$

In this case, the Fermi level is divided into E_{Fp} and E_{Fn} for holes and electrons. The quasi-Fermi levels, E_{Fp} relative E_V , and E_{Fn} relative E_C , still determine species concentration, with the quasi-Fermi levels substituting E_F in the equation. (2.7) [32].

2.3 Solar Cell Parameters

These are the major characteristics used to characterize the performance of solar cells. These parameters are based on lighted J-V characteristics. It can be used to assess conversion efficiency [32].

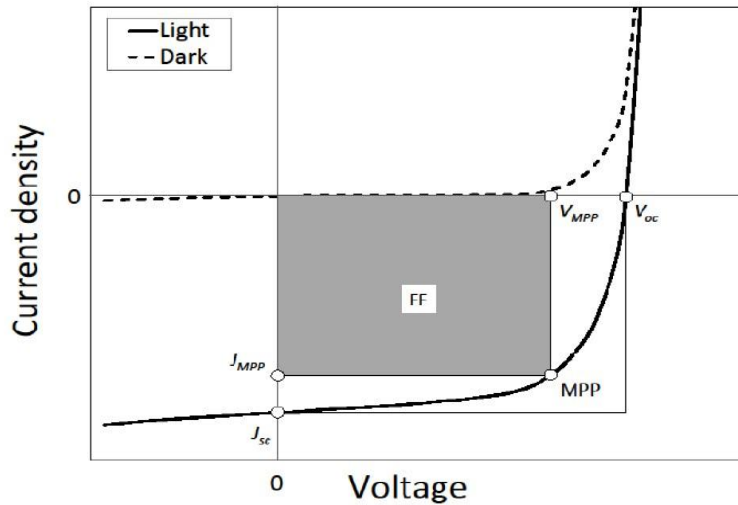


Figure 2.3: J-V Characteristics of p-n junction with and without Illumination [32].

2.3.1 Short Circuit Current Density

A short circuit's current When the solar cell's electrodes are short, J_{sc} flows through the external circuit. The photon flux incident on a solar cell determines the short circuit current. For normal solar cell measurements, the AM1.5 spectrum is used. The I_{sc} value is related to solar cell area. Short-circuit current density (SCCD) is widely used to characterize a solar cell's greatest current output to avoid proportionality with I_{sc} . The best current a solar cell can produce is determined by its optical properties, such as absorbing layer absorption. In an ideal environment, $J_{sc} = J_{ph}$, as shown in Eq (2.13),

$$J(v_a) = J_{rec}(v_a) - J_{gen}(v_a) = J_0 e^{\frac{qv_a}{k_B T}} - J_{ph} \quad (2.13)$$

In the case of a perfect diode (no surface recombination) and uniform generation, minority carrier diffusion lengths are the crucial material factors to estimate J_{ph} .

$$J_{ph} = qG(L_n + w + L_p) \quad (2.14)$$

L_N and L_P are the minority-carriers diffusion length for electrons and holes, respectively, and W is the width of the depletion region [32].

2.3.2 Open Circuit Voltage

The open-circuit voltage is the voltage at which no external current flows. It is the maximum output voltage of a solar cell. Dark current density = photocurrent density = V_{oc} . If there is no net current, V_{oc} is proportional to the photogenerated current density.

$$V_{oc} = \frac{k_B T}{q} \ln \left(\frac{J_{ph}}{J_0} + 1 \right) \quad (2.15)$$

J_0 in equation (2.12) shows that V_{oc} is reliant on the solar cell's saturation current density and photogenerated current. The crucial effect is the change in the saturation current, which can vary by order of magnitude. The saturation current density, J_0 , is determined by recombination. Thus, V_{oc} is a device's recombination rate [32].

2.3.3 Fill Factor

The fill factor is the ratio of maximum power ($P_{max} = J_{mpp}V_{mpp}$) to the product of V_{oc} and J_{sc} (Figure 2.3),

$$FF = \frac{J_{mpp}V_{mpp}}{J_{sc}V_{oc}} \quad (2.16)$$

On the J-V characteristic of a solar cell, the subscript "mpp" indicates the solar cell's maximum power point (MPP). It is vital to run solar cells (or photovoltaic modules) at MPP to optimize photovoltaic system performance. Maximum Power Point Tracking is used to achieve this (MPPT). Assuming the solar cell behaves like an ideal diode, the fill factor can be calculated as the open-circuit voltage function [32].

$$FF = \frac{V_{oc} - \log(V_{oc} + 0.72)}{V_{oc} + 1} \quad (2.17)$$

2.3.4 Power Conversion Efficiency (PCE)

The maximum produced power divided by the incident power is the efficiency of conversion. As previously stated, solar cells are evaluated using the STC, which assumes an AM1.5 spectrum and an $I_{IN} = 1000 \text{ W/m}^2$ irradiance [32].

$$\eta = \frac{P_{out}}{P_{in}} = \frac{J_{SC}V_{OC}FF}{P_{in}} \quad (2.18)$$

2.3.5 External Quantum Efficiency (EQE)

Quantum efficiency outside *EQE* is the percentage of photons that hit the solar cell and produce electron-hole pairs in the absorber. It is calculated by illuminating the solar cell with monochromatic light of the desired wavelength and measuring the photocurrent I_{ph} . The external quantum efficiency is then calculated as,

$$EQE(\lambda) = \frac{I_{ph}(\lambda)}{q\psi_{ph,\lambda}} \quad (2.19)$$

Where q is the basic charge and $\psi_{ph,\lambda}$ is the photon flux impacting on the solar cell. Because I_{ph} is dependent on the bias voltage, it must be kept constant during the test. An *EQE* comparison of a calibrated photo diode to the light source typically yields the photon flow [32].

2.4 Equivalent Circuit of Solar Cell

Figure 2.4 (a) shows a simple analogous circuit with a diode and a current source connected in parallel. In practice, the FF is influenced by resistance R_s and shunt resistance R_{SH} . These parameters' impact on the solar cell's J-V characteristic can be evaluated using Figure 2.4's analogous circuit (b). In the one-diode equivalent circuit with series and shunt resistances,

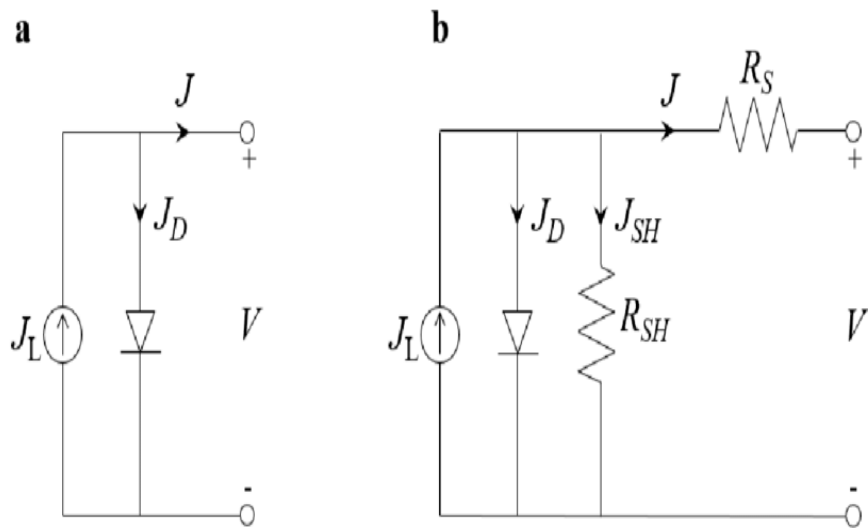


Figure 2.4: The equivalent circuit of (a) an ideal solar cell; and (b) a solar cell with series resistance R_s and shunt resistance R_{SH} [32].

2.5 Air Mass

A light journey through the atmosphere, normalized to the shortest path possible (when the sun is directly overhead). In the atmosphere, light is absorbed by air and dust, reducing its strength. The word "Air Mass" means,

$$AM = \frac{1}{\cos \theta} \quad (2.20)$$

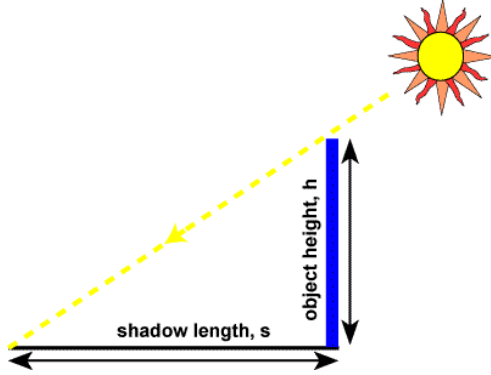


Figure 2.5: Air Mass Determination [33].

Air mass is the ratio of the length of the hypotenuse and the object height h , and from Pythagoras's theorem we get,

$$AM = \sqrt{1 + \left(\frac{s}{h}\right)^2} \quad (2.21)$$

Here θ is the angle from the vertical (zenith angle). When the sun is directly overhead, the Air Mass is 1 [31].

2.6 Solar Spectrum

Solar radiation produces energy in the form of electromagnetic waves. Longer wavelengths (like infrared) carry less energy (for example, visible light or ultraviolet). The spectral distribution graph depicts the relative weights of various wavelengths against all other wavelengths in W/m^2 . (wavelength). Diagram of a solar beam just beyond the earth's atmosphere's entrance. The visible spectrum is the most powerful, but there are numerous shorter and longer wavelengths [33].

Irradiance [W/m^2]: The total contribution of all wavelengths within the spectrum to the intensity of solar radiation impacting a surface, given in Watts per m^2 of surface.

Power [W]: Momentary total irradiance incident on a particular area.

Atmospheric absorption modifies the sun's spectrum. The power density of AM1 (normal incidence) is 925 W/cm^2 , whereas AM1.5 (45° above the horizon) is 844 W/m^2 . Absorption at various photon energies causes spectrum abnormalities. As illustrated in Figure 4.8.2, the cumulative photocurrent is energy dependent. [33]

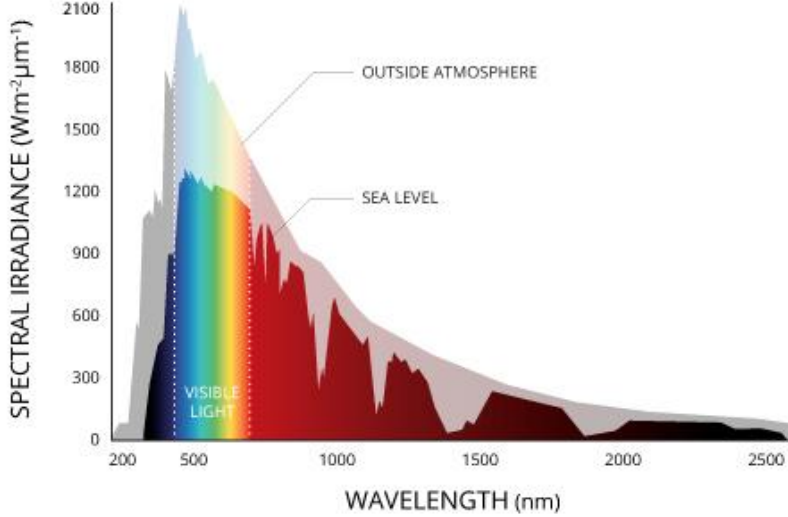


Figure 2.6: AM 1.5 Solar Spectrum [34].

2.7 Restrictions and Losses

Assuming a perfect system, Shockley and Queisser [35] determined the theoretical upper limit of a solar cell's power conversion efficiency. Also taken into consideration is radiative recombination, which must exist owing to thermal equilibration. Thermalization losses result from excess energy dissipating as heat when $E > Eg$. A single bandgap energy of roughly 1.1 eV was discovered to give somewhat more than 30% efficiency in the original Shockley-Queisser limit calculation. Optimal bandgaps vary between 1.1 and 1.4 eV depending on the spectra utilized, although they are always somewhat above 30%. Additional recombination, including defect assisted recombination (SRH) and for highly doped semiconductors, Auger recombination; optical losses, such as reflectance, parasitic absorption, and incomplete absorption; and resistive losses, such as dc and ac voltage drop across a material's contact (SRH formalism). In paper II, we focused on recombination loss mechanisms and their impact on device performance. It is vital to note that SRH recombination is important in thin films.

$$U = \frac{\sigma_n \sigma_p v_{th} N_T (np - n_i^2)}{\sigma_n \left[n + \eta_i \exp\left(\frac{E_T - E_i}{k_B T}\right) \right] + \sigma_p \left[p + \eta_i \exp\left(\frac{E_i - E_T}{k_B T}\right) \right]} \quad (2.22)$$

and any recombination rate is proportional to the total number of free carries, as a rule of thumb.

$$U \propto np - n_i^2 \quad (2.23)$$

In the SRH formalism (12), σ are capture cross-sections, and V_{th} is thermal velocity, N_T and E_T are the defect concentration and energy level respectively above the valence band. It's vital to remember that recombination routes are seldom saturated, thus they all help recombination in different ways depending on how effective and accessible the charge carriers are. It is extremely advantageous to utilize a modeling program to map the real recombination currents in order to acquire precise findings. Minority carrier diffusion length L is connected to U via minority carrier lifespan and is used throughout this thesis and associated works (e.g., electrons for a p-type semiconductor).

$$\tau_n = \Delta n U^{-1} \quad (2.24)$$

Such that,

$$L_n = \sqrt{D_n \tau_n} \quad (2.25)$$

Statistically, a carrier will travel the entire length of L without external disruption. The diffusion length, along with the SCR width, impacts the efficiency of collecting minority carriers, as detailed in papers II, IV, and V. Sze and Ng [36] provide more semiconductor device physics theory, whereas Green [37] describes PV physics.

2.8 Evolution of Solar Cell

Differentiating between single-junction and multi-junction solar panels or first, second, and third generations is a common method. Single-junction and multi-junction solar panels have different layers that absorb sunlight. However, generation classification focuses on solar panel materials and efficiency [41].

2.8.1 1st Generation Solar Cells

These are the most common solar panels used in conventional settings, composed of monocrystalline silicon or polysilicon.

2.8.1.1 Monocrystalline Solar Cells

The purest solar panel is monocrystalline silicon. Their consistent black appearance and rounded edges immediately identify them. Its high efficiency is due to the silicon's purity, with the most recent panels reaching over 20%. Monocrystalline panels produce the most power, are the smallest, and lastly the longest. That makes them the priciest. Their resistance to high temperatures is another benefit.

2.8.1.2 Polycrystalline Solar Cells

Poly-Si solar panels are easily identified by their square shape, non-cut angles, and blue speckled appearance. Like monocrystalline panels, they are manufactured by melting raw silicon. This results in lower final prices, reduced efficiency (about 15%), less space efficiency, and shorter lifespan due to increased sensitivity to hot temperatures. However, the distinctions between monocrystalline and polycrystalline solar panels are minor, and the choice is very contextual. The first choice saves space but costs more, although the power output is the same.

2.8.2 2nd Generation Solar Cells

Many thin-film solar cells are primarily utilized in photovoltaic power plants, incorporated into buildings and tiny solar systems.

2.8.2.1 Thin-Film Solar Cells (TFSC)

Solar panels with thin-film technology are created by depositing one or more photovoltaic films (such as silicon, cadmium, or copper) over a substrate. These solar panels are the easiest to build, and because less material is required for production, they are more economical than others. Additionally, they are flexible, offering up several possibilities for alternate applications

and are less susceptible to high temperatures. The primary disadvantage is that they use a great deal of space, rendering them unsuitable for household installations. Additionally, they come with the lowest warranties due to their lower lifespan than monocrystalline and polycrystalline solar panels. They can, however, be an advantageous alternative when a large amount of space is available for solar panels.

2.8.2.2 Amorphous Silicon Solar Cell (A-Si)

Most pocket calculators use amorphous silicon solar cells. Thin-film solar panels employ triple-layer technology. "Thin" here means 1 micrometer (one-millionth of a meter). A-Si-Cells are less efficient (7%) but cheaper than crystalline silicon cells.

2.8.3 3rd Generation Solar Cells

Third-generation solar panels use several thin-film technologies; however, most are still in the research and development stage. Some of them create energy via organic materials, while others do so via inorganic elements (CdTe, for instance).

2.8.3.1 Biohybrid Solar Cell

Biohybrid solar cells are a new type of photovoltaic cell still in development. Vanderbilt experts found it. The novel technology uses photosystem 1 to mimic the natural process of photosynthesis. The American Journal of Optics and Photonics contains more information on how the biohybrid solar cell works. It explains how these cells work in detail. Many of the components used in this cell originate from prior generations. However, by combining the photosystem 1 layers, chemical energy conversion becomes significantly more efficient (up to 1000 times more efficient than 1st generation types of solar panels).

2.8.3.2 Cadmium Telluride Solar Cell (CdTe)

This photovoltaic technique uses Cadmium Telluride, which allows the fabrication of solar cells at a low cost, resulting in a shorter payback period (less than a year). This is the tiniest water-intensive solar technology. Due to their short energy payback period, CdTe solar cells help reduce carbon emissions. The only disadvantage of using Cadmium Telluride is that it is toxic when inhaled. This is a major issue in Europe because many people are wary of using the technology behind this solar panel.

2.8.3.3 Concentrated PV Cell (CVP and HCVP)

These cells work like solar panels. Multi-junction solar panels give up to 41% photovoltaic system efficiency. Curved mirrors, lenses, and occasionally cooling devices bundle the sun's rays. As a result, CVP cells have become one of the most efficient solar panels on the market, with up to 41% efficiency. The CVP solar panels are effective if they face the sun at the optimum angle. A solar tracker embedded in the solar panel tracks the sun to achieve high efficiency [38,39].

2.9 Thin Film Solar Cells Technology

The Cu₂S/CdS thin-film solar cell achieved 10% efficiency in 1981 [43]. In the 1970s and 1980s, CuInSe₂, CdTe, and a-Si were the most prevalent solar cell materials, all of which could

obtain a 10% efficiency. It was believed that thin films would be mass produced and cost \$1 per watt per year. During the 1990s, performance of thin film solar cells improved with increasing CdTe and a-Si concentrations. It was also prompted by the mid-1990s discovery of C-Si. In the early 1900s, photovoltaic (PV) manufacturing grew by over 35% yearly. Compared to 2007, global solar cell production increased to 6.85 GW. In 2008, thin film output reached 0.89 GW, up 120% from the previous year.

Lack of new c-Si and mc-Si modules has aided thin-film technology development. One-gigawatt production capacity has nearly doubled. This technology has achieved the industry's lowest manufacturing cost per watt of less than \$1 per watt. Applied Materials, Oerlikon, and Sharp are the leaders in silicon production. Global Solar, Wurth Solar, Showa Shell, and Honda have all entered the CuInSe₂ module market. Thus, several new companies developing CuInSe₂, CdTe, and Si-based technology have received venture capital funding. The market share of thin-film photovoltaic modules is expected to rise. Commercial thin-film modules have efficiencies of 12–19%. The most efficient modules are CuInSe₂ based (9 to 12%), followed by CdTe based (9 to 11%) and -Si based (5 to 8%). Production-level thin-film technologies like c-Si are still stuck in the 1980s. The tables exhibit devices made of single and multicrystal Si, CdTe, and CuInSe₂. Because of capacity growth, CdTe, the most commercially sophisticated technology, has maintained its greatest performance value.

Single-crystalline Si cells are over 85% efficient, while CuInGaSe₂ cells are around 70% efficient (not shown on graph). CdTe is only about 55% efficient, therefore considerable scientific improvements are necessary to fully utilize its potential. To evaluate silicon photovoltaic technology, we need a standard with many junctions. The difference between the best cell and module shows technical readiness for production. However, multijunction a-Si and c-Si modules achieve roughly 80% efficiency, whereas mc-Si modules achieve approximately 75% efficiency.

Many thin-film modules have a substrate, TCO, or grid, as well as metal connectors. The substrate can be glass, flexible plastic, or metal foil. Ultrathin TCOs like ITO, SnO₂, and ZnO are virtually often employed as superstrate. Glass or flexible substrates are available for custom modules; CdTe modules are always on glass. CuInSe₂ modules with Mo back contacts use glass substrates, whereas a-Si and CuInSe₂ modules use flexible metal foils or polyimide substrates (web). Aside from polyimide and stainless-steel substrates, several start-ups have recently researched CuInSe₂ in polyimide and metal webs. Unlike c-Si, which uses individual wafer cells and manually connects them with stringing techniques [39].

Chapter 3

Literature Review

3.1 Properties of the Materials

3.1.1 FeS₂

Pyrite, technically known as an iron disulfide, is the most prevalent sulfide mineral found in nature. The crystal structure is like that of fluorite. Iron disulfide has a yellow-brass, metallic sheen that is occasionally mistaken for gold. Due to this erroneous identification, it is frequently referred to as "fool's gold". Pyrite was employed as an ignition source for early weapons because of the sparks emitted when hit on metal. Pyrite is also utilized in the production of sulfur dioxide, a gas used in the paper industry and in the manufacture of sulfuric acid [40].

At room temperature, FeS₂ crystallizes as pyrite which has a simple cubic-SC Lattice with the space group Pa3(Th6) with a lattice constant of 5.4160 [41,42,43]. The crystal structure of pyrite is best described in terms of the NaCl structure with iron atoms occupying the sublattices and sulfur atom pairs at the center of gravity as shown in Figure 3.1. The sulfur dumbbells are oriented parallel to the (111) axis. Their bond length is still shorter than the Fe-S distance of 2.265 at 2.161.

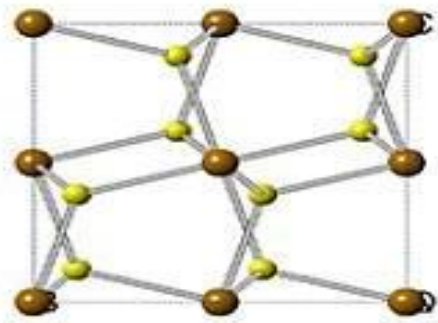


Figure 3.1: FeS₂ Crystal Structure [41].

One sulfur and three iron atoms tetrahedrally coordinate the sulfur atoms, whereas the six sulfur atoms closest to each iron site form deformed octahedra. The local symmetry at these points changes from cubic (Oh) to trigonal due to the octahedra's deformations (C3i). Due to the production of the (111) sulfur pairs, the distorted FeS₆ octahedra are joined by shared corners and have rotated away from the Cartesian axes by roughly 23°. The square-planar coordination of the iron atoms is not disrupted by the formation of the (111) sulfur pairs. Sulfur atoms, on the other hand, generate squares that decrease and rotate. Because the dumbbells are orientated according to the cubic point group, the underlying Bravais lattice is no longer face centered but simple cubic, and the unit cell contains four formula units. However, as shown below, certain properties of the electrical structure may be described in terms of the face-centered-cubic (FCC) lattice. The space group Pa3 (Th6) is unique among the 230 space groups, according to

Bradley and Cracknell. It is neither a member of a pair of isomorphic space groups nor an invariant subgroup of any larger space group based on the simple cubic Bravais lattice. [44]

3.1.2 CuBi₂O₄

The crystal structure of CuBi₂O₄ is a three-dimensional array of [CuO₄]⁶⁻ square-planar units staggered along the c-axis and separated by Bi³⁺ ions. High-temperature superconducting cuprates, unlike isoelectric prototypes, are superconducting at high temperatures. CuR₂O₄ (where R is a trivalent rare-earth element), where the [CuO₄]⁶⁻ square planar units form infinite two-dimensional layers. CuBi₂O₄ with its isolated [CuO₄]⁶⁻ units is unlikely to be superconducting due to this structural property.

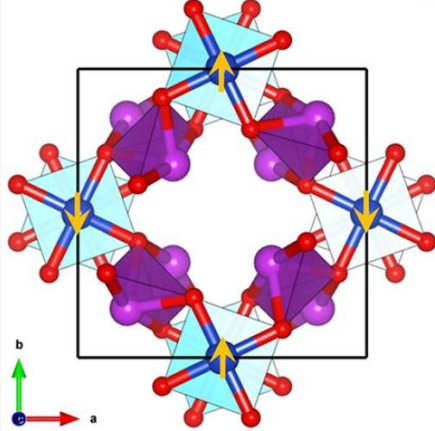


Figure 3.2: CuBi₂O₄ Crystal structure [45].

However, CuBi₂O₄ has shown potential for photoelectrochemical (PEC) solar energy conversion into chemical fuels [45-47]. This material's photocathodes have been reported to yield photocurrent densities of 1.0 mA/cm² at 0.0 V vs the reversible hydrogen electrode (RHE) with a Faradaic efficiency of 91%. They are important in causing desired material features including visible light absorption and p-type conductivity in the ternary oxide CuBi₂O₄ [48,49]. Thus, knowing the VBM's elemental makeup can help designers improve materials' qualities. The main limitations of CuBi₂O₄ are the lack of photo corrosion stability in aqueous solutions and poor charge carrier transport characteristics [49,50]. Due to these constraints, the development of CuBi₂O₄ based photoelectrodes will be dependent on improving interfacial electric contacts with charge protection and transport layers. To overcome efficiency losses caused by unfavorable charge carrier dynamics and transport, interface energetics must be engineered.

A detailed description of CuBi₂O₄'s electronic structure and electron energetics utilizing X-ray photoemission, X-ray absorption, and density functional theory calculations. The Bi 6s and Cu 3d electrons contribute to the valence band via hybrid electronic states with O 2p, according to several theoretical analyses based on DFT calculations [49,50,51]. The energy levels of the metal orbitals' contributions to the valence band, on the other hand, are a point of contention. Janson et al.⁶ and Di Sante et al. [52] found similar findings. suggest that while Sharma et al.² calculated that Bi 6s and Cu 3d have comparable contributions to the VBM, the Bi contribution is negligible, and thus an effective one-band model is appropriate for the description of low-lying excitations in CuBi₂O₄.

They correctly predict electrical properties and soft X-ray photoemission spectra of low-dimensional cuprates [50] because these models allow for configurations, interactions, and final states with more than one d hole (i.e., Cu 3d8). The excitation of low-lying energy levels (i.e., the VBM) in $[CuO_4]_6$ clusters is coupled to a singlet state ($3d^9L$, L = ligand hole). 9,10 This singlet state has a high stabilization energy as a result of its hybridization with d8 and d10 L2 structures, and it has a big impact on cuprate charge mobility and doping stability.

3.1.3 GaAs

The chemical symbol for gallium arsenide is GaAs. GaAs is the name for a gallium-arsenic compound. When these two elements combine to make a III-V direct bandgap semiconductor with a zinc blend crystal structure, the result is a III-V direct bandgap semiconductor with a zinc blend crystal structure. A kind of gallium arsenide is gallium arsenide.

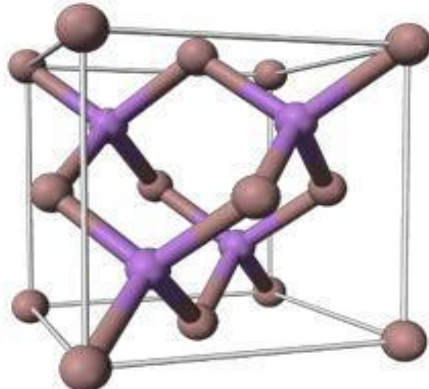


Figure 3.3: GaAs Crystal Structure [51].

Three approaches for industrial manufacturing include the vertical gradient freeze (VGF) technique, the Bridgman-Stockbarger technique, and liquid encapsulated Czochralski (LEC) growth. The VGF process is the most frequent way to make GaAs wafers. The procedure includes growing homogeneous crystals to the required diameter, thinly slicing them to extremely tight tolerances, rounding the form factors on the edges, polishing, and packaging the wafers. The Bridgman-Stockbarger process involves growing crystals in a horizontal zone furnace that allows gallium and arsenic vapors to react, then depositing the released molecules on a seed crystal chilled at the furnace's end. To make high-purity single crystals with semi-insulating properties, the LEC growth method is used. Wafers and integrated circuits (ICs) have a wide range of applications. GaAs is used in integrated microwave circuits (ICs), monolithic microwave integrated circuits (ICs), LEDs, laser diodes, and solar cells. GaAs is particularly helpful in high-speed circuits, and ultrathin GaAs chips are used at the front end of many systems [51].

3.2 FeS₂ Based Solar Cell Technology

Iron pyrite (FeS₂) has a number of electrical and optical properties that make it a good absorber material for solar cells. For example, it has a bandgap of 0.95 eV (to achieve solar energy conversion efficiencies close to the Shockley–Queasier limit), long minority carrier diffusion

lengths (100–1000 nm), a high absorption coefficient proportional to thin-film thickness for complete light absorption (a 100 nm thick film absorbs >90 percent of sunlight below the bandgap), and electron mobility of up to 360 cm. FeS₂ has a lot of potential for use in solar cells, especially as a thin-film photovoltaic (PV) material in combination with other thin-film photovoltaic (PV) materials as CdTe, CuIn_{1-x}Ga_xSe₂ (CIGS), and hybrid perovskites [53–55]. FeS₂ could produce electricity at the lowest cost of any solar cell material currently available. A comparison study [56] compared the annual power generation capacity (TW) and manufacturing cost of 23 different materials, including Si (per W). FeS₂ outperforms all of them. Most importantly, FeS₂ outperforms Si in all aspects. The energy required for extraction (24 kWh kg⁻¹ for Si vs 2 kWh kg⁻¹ for Fe), the cost of extraction (\$1.70 per kg for Si vs \$0.03 per kg for Fe), the photon flux absorption coefficient (FeS₂ has a two-orders-of-magnitude higher absorption coefficient), and the low Levelized cost of the raw material per peak Watt (0.039 per W for Si [57]. The cost of producing Si has plummeted, and new thin-film solar materials have appeared (hybrid perovskites and copper zinc tin sulfide, CZTS). FeS₂'s intrinsic material consumption and extraction cost, on the other hand, are both exceedingly low. Assume FeS₂ is produced in the same country as Si with the same wages, electricity prices and tax laws. In such circumstances, FeS₂ is projected to be more cost-effective in photovoltaic technology than Si.

Given the cost of generating modules with interconnects/framework and the additional system expenditures associated with installation, the power conversion efficiency (PCE) must be much greater than 4% to be competitive. FeS₂ is predicted to require achieving efficiencies equivalent to those of other thin-film technologies to be economically feasible, given that raw material costs make up such a small percentage of overall module and system prices.

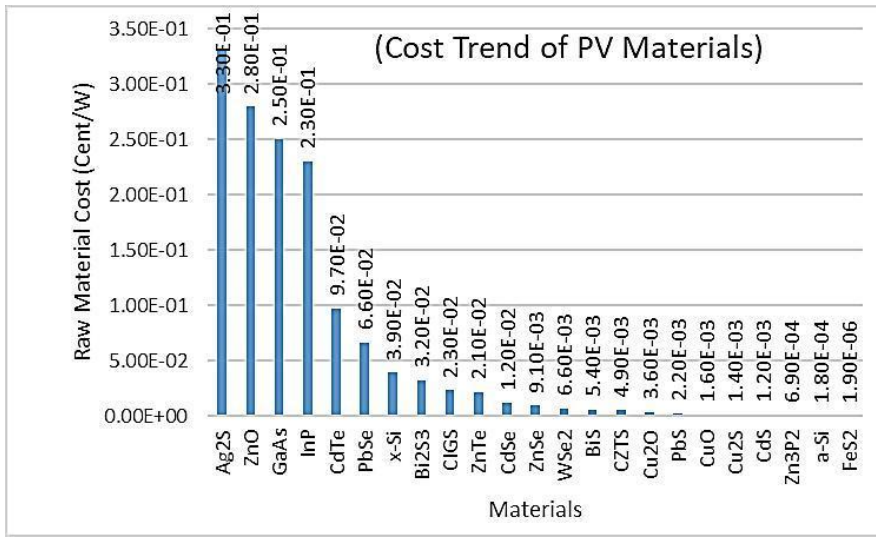


Figure 3.4: Price Comparison of Various PV materials [24,25].

FeS₂ solar cells have never reached a PCE of more than 2.8 percent since its inaugural presentation, despite global recognition and a three-decade-long research effort. This value was achieved using a liquid junction I/I₃ electrolyte in a photoelectrochemical cell, and no PCE has been confirmed in an accredited laboratory. Solid-state devices, on the other hand, have shown to have a significantly lower PCE. The extremely low open-circuit voltage, V_{oc} (typically 200

mV), contributes to the low PCE [57]. Bulk or near-surface non-stoichiometry, mid gap defects, thermionic-field emission, significant dark current, metallic FeS like sulfur layer, and other factors all contribute to the low V_{OC} . As a result, basic studies on growth, structural and electrical characteristics, FeS_2 passivation, and the appropriate window and back surface layer that will offer greater built-in potential to minimize dark current and therefore higher V_{OC} are required to increase V_{OC} and hence PCE.

Sulfurization of an iron film is sputtering, flash evaporation, molecular beam epitaxy, electrodeposition. High throughput, large-area processing methods including printing, roll coating, slit casting, or spraying, as well as solution procedures that maintain atmospheric pressure, may provide cost and scalability benefits over vacuum-based technologies used in the PV manufacturing sector [57].

3.3 CuBi₂O₄ Based Solar Cell Technology

In recent years, copper-based ternary oxide semiconductors with narrow energy band gaps have attracted a lot of interest as a photocathode material for solar energy conversion [58,59]. Because to its low cost and ease of use, p-type CuBi₂O₄ has been identified as one of the most promising photocathode materials for solar cell technology [60-62]. CuBi₂O₄ has a low energy band gap of 1.4 to 1.8 eV [63-65], which is close to the ideal value for solar cell applications, a high optical absorption coefficient of more than 10^4 cm^{-1} [66], is non-toxic, and has sufficient resources. Cu is a chemical element with atomic number 29, group 11, period 4 in CuBi₂O₄ substance, and it is a soft, malleable, and ductile metal with extremely high thermal and electrical conductivity [67]. Bismuth is the only metal that has been proven to be inherently diamagnetic. Bismuth (Bi) is a silvery metal that is soft, crystalline, and brittle with low thermal conductivity. It's resistant to both oxygen and water. Bismuth has an atomic number of 83 and belongs to group 15 [68]. The colorless nonmetallic chemical element oxygen (O) is found in the periodic table [69]. Electric discharge in oxygen or the impact of UV radiation on oxygen in the stratosphere can create reactivity in oxygen. Oxygen is a powerful oxidizer with the second highest electronegativity among the reactive elements [20]. Previous investigations [70] looked into a variety of heterojunction designs based on CuBi₂O₄ materials. The photocatalytic performances of CuBi₂O₄/O₃, CuBi₂O₄/CeO₂, CuBi₂O₄/SnO₂, CuBi₂O₄/g-C₃N₄, CuBi₂O₄/NiO and CuBi₂O₄/UO p-n heterojunction structures produced by hydrothermal synthesis and pulsed laser de In addition, for solar applications, a high-density p-type CuBi₂O₄ thin-film on FTO glass substrate is created using a spin-coating approach [70].

Due to its high absorption coefficient, narrow energy band gap, and nontoxicity, the thin film of ternary oxide semiconductor CuBi₂O₄ is projected to be used as one of the most promising absorber materials in TFSCs. Furthermore, solution techniques may be used to create thin films of CuBi₂O₄ material in heterojunction structures, which would be particularly useful for cost-effective and high-performance light harnessing elements when compared to standard absorber materials. However, there are few publications on thin-film solar cells based on CuBi₂O₄ that have a low light conversion efficiency [28]. As a result, a novel type of thin-film heterojunction solar cell with sufficient photovoltaic performance is predicted to be investigated using the CuBi₂O₄ Material as an absorber layer. As a result, it's crucial to comprehend photo-generated

charge carrier transport in CuBi₂O₄ based thin-film heterojunction devices. To make the CuBi₂O₄ based TFSC a reality.

3.4 GaAs Based Solar Cell Technology

Gallium arsenide is a critical semiconductor material for high-efficiency, low-cost solar cells. It's employed in both single-crystalline and multi-junction thin film solar cells [73]. The Venera 3 mission, which was launched in 1965, was the first spacecraft to employ GaAs solar cells. GaAs solar cells were chosen because of their superior performance in high-temperature environments. [77] For the same reason, GaAs cells were employed in the Lunokhod rovers. In 1970, a team led by Zhores Alferov in the Soviet Union created GaAs heterostructure solar cells with significantly better efficiency [77]. In the early 1980s, the best GaAs solar cells exceeded classic crystalline silicon solar cells in terms of efficiency. In the 1990s, GaAs solar cells overtook silicon as the most prevalent cell type for photovoltaic arrays aboard spacecraft. Solar cells with dual and triple connections based on GaAs with Germanium and indium gallium phosphide layers were further developed. Developed as the foundation for a triple-junction solar cell with a record efficiency of more than 32% and the capacity to work in light intensities of up to 2,000 suns. Opportunity and the Spirit Solar cells of this sort were used to power the Mars Exploration Rovers while they explored the Martian surface. GaAs is also utilized in the solar panels of many solar automobiles. With an efficiency of 29.1 percent, GaAs-based devices hold the global record for the highest-efficiency single-junction solar cell. (As of the year 2019). This remarkable efficiency is attributed to the extremely high-quality GaAs epitaxial growth, the AlGaAs surface passivation [77], and the thin film design's support for photon recycling [99].

Chapter 4

Material & Methodology

4.1 SCAPS-1D

In this project SCAPS 1D was used which is very popular solar cell simulation software among students and scientists. It can affect solve thin film and multi-junction solar cells. The various defect can be added during design. The scope of this software is enormous, and we took advantage of a few of its features. SCAPS is a one-dimensional solar cell modeling tool from Gent University (ELIS). Alex Niemegeers, Marc Burgelman, Koen Decock, Johan Verschraegen, and Stefaan Degraeve contributed.

4.1.1 Basics of SCAPS 1D

SCAPS is a Windows-based software created with National Instruments' Lab Windows/CVI. A 'Panel' is what we call it in LW/CVI (other software calls it a home page, or a pop-up...). The 'Action Panel' is the first thing you see when you start SCAPS. [78].

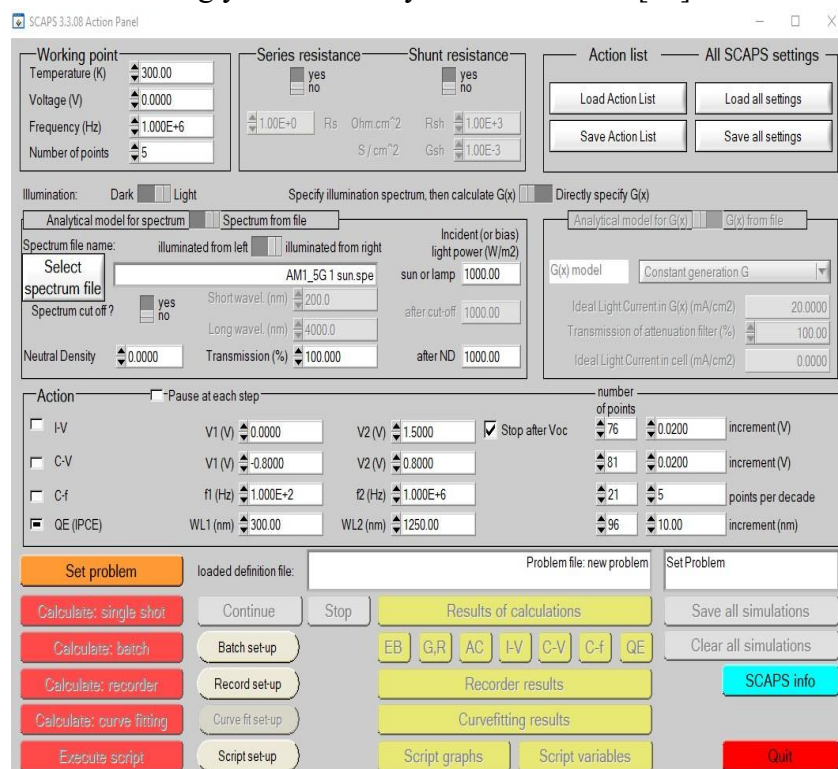


Figure 4.1: Action Panel of SCAPS-1D.

4.1.2 Editing A Solar Cell Structure

When 'Set Problem' is clicked on the action panel, 'Solar cell definition' displays. This panel lets you create/edit solar cell structures and save/load definition files. *.def definition files may be examined in notepad. Despite being self-explanatory, manually editing these files is recommended. We can change the layer, contact, and interface characteristics by clicking on

the corresponding box in Figure 3.1. Layers can also be added by clicking the 'add layer' button. [78].

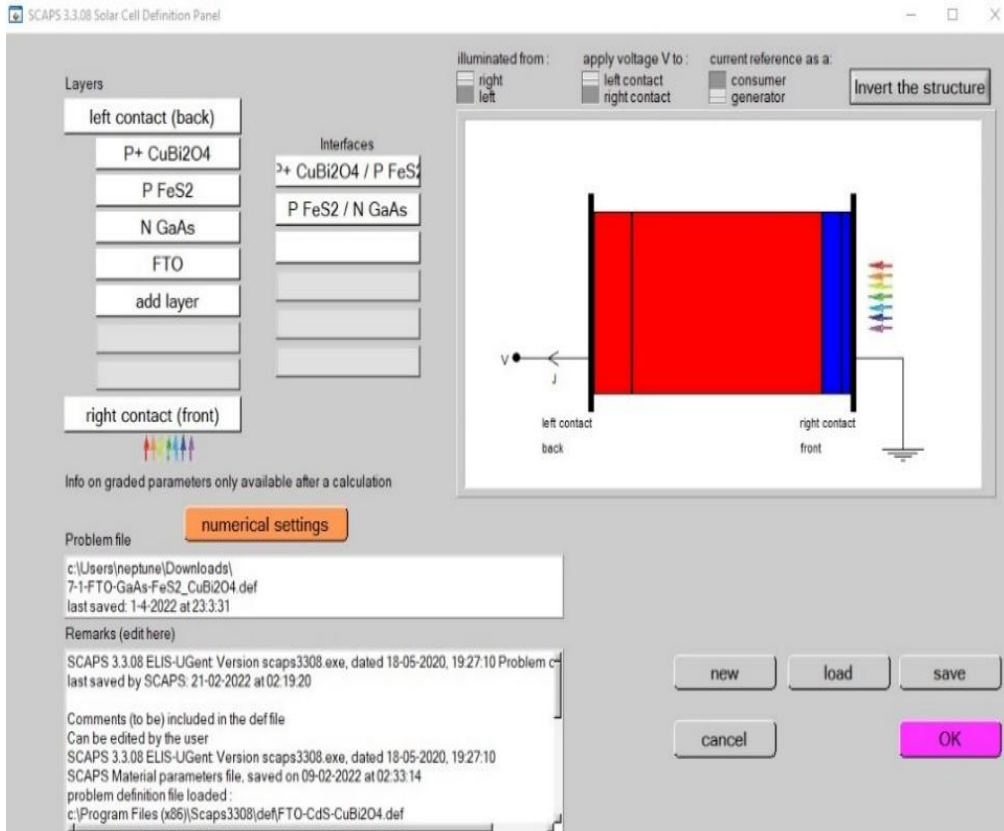


Figure 4.2: Layer Editing Panel.

4.1.3 Mathematical Model in SCAPS-1D

4.1.3.1 Calculations for A Single Shot

SCAPS solves the one-dimensional semiconductor equations in conjunction with the constitutive equations (4.1) & (4.2). A system of coupled differential equations is formed when coupled differential equations are utilized. SCAPS solves the steady-state and small signal solutions of this system numerically. Initial discretization (creating a mesh). As needed, a steady-state working point scenario and minor signal analysis are created. [78].

$$J_p = q(\mu_p \mathbf{p} \cdot \boldsymbol{\xi} - D_p \nabla \cdot \mathbf{p}) \quad (4.1)$$

$$J_n = q(\mu_n \mathbf{n} \cdot \boldsymbol{\xi} - D_n \nabla \cdot \mathbf{n}) \quad (4.2)$$

1.3.2 Contacts

Figure 4-3 shows how to modify contact characteristics by pressing the front or rear contact button on the cell definition panel. User can access metal work function m . (for majority carriers). "Flat bands" are another option. SCAPS calculates the metal work function m for each temperature to create flat bands. Previous SCAPS versions used a simpler algorithm.

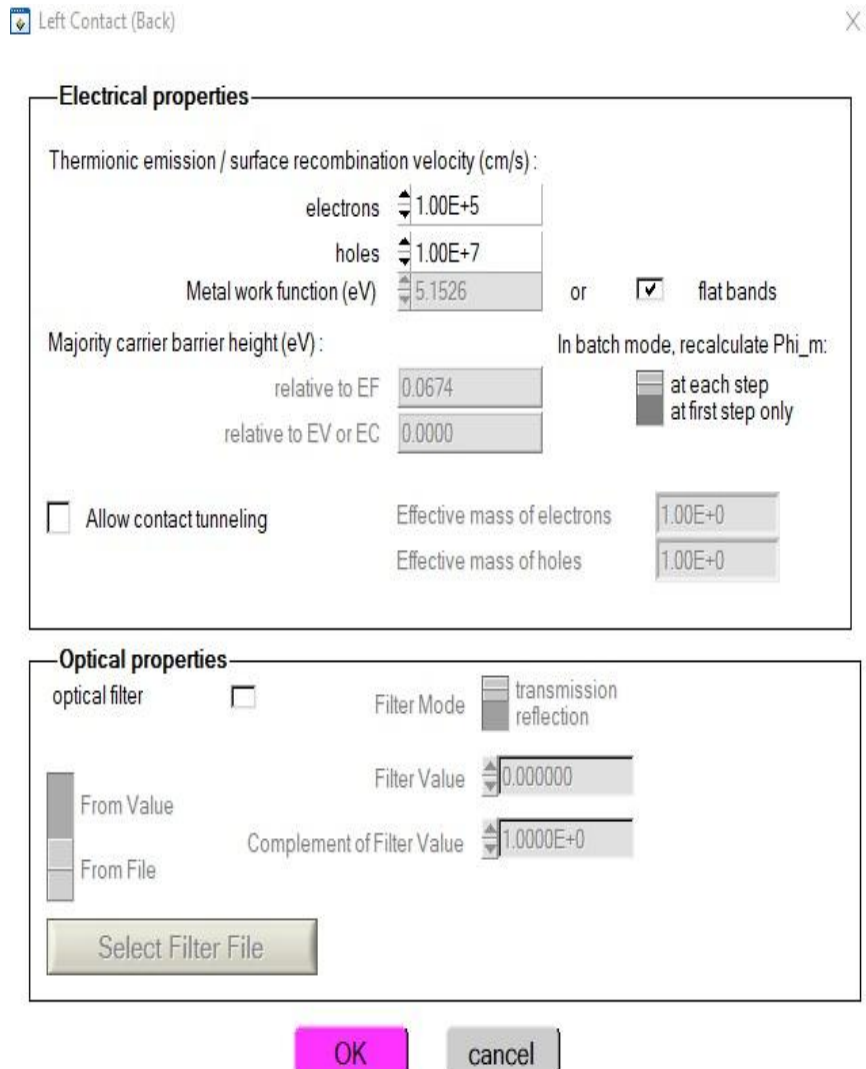


Figure 4.3: Contact Editing Panel.

The method mentioned below was employed equation (4.4) is used when the layer adjacent to the contact is n-type, Eq. (4.5) is used when the layer is p-type and equation (4.6) is used when the layer can be regarded intrinsic [78].

$$\phi_m = \chi + k_B T \ln \left(\frac{N_C}{N_A - N_D} \right) \quad (4.3)$$

$$\phi_m = \chi + k_B T \ln \left(\frac{N_C}{N_D - N_A} \right) \quad (4.4)$$

$$\phi_m = \chi + k_B T \ln \left(\frac{N_C}{n_i} \right) \quad (4.5)$$

4.1.3.3 Adding defects

A semiconductor layer can have 7 flaws. Selecting each flaw's Add/Edit button reveals the 'fault characteristics panel,' Figure 3.24. We may right-click on one of the "fault summary text boxes" to delete, duplicate, or add a problem. Splitting a fault is useless, hence it's not permitted. [78]

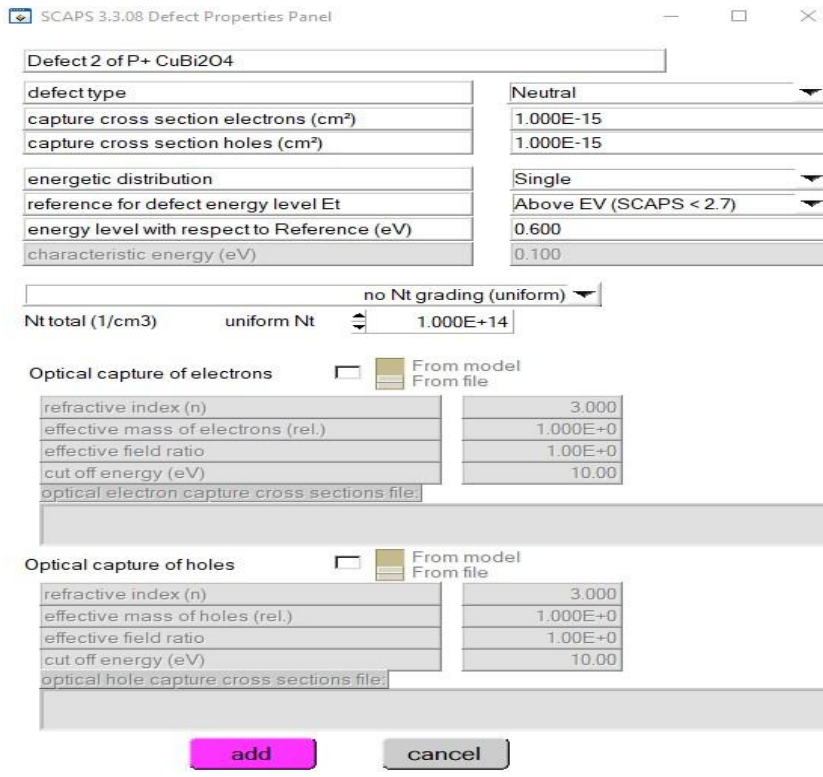


Figure 4.4: Defect Simulation Panel.

4.1.3.4 A neutral defect

"Neutral" defect idealizes a defect that contributes to Shockley-Read-Hall recombination but not space charge. In a "neutral" defect, only the product of N_t and N_c affects dc and ac carrier lifetimes. for example, $t_n = 1 / (t_n \cdot N_t \cdot V_{th})$: in this situation, the defect canters contribute to recombination but not to the space charge. This form of defect may be used to set electron and hole lifetimes without defining a defect density that influences the space charge. In other words, a neutral flaw does not exist in reality; it is only an idealization used to guide through the process of developing a model [78].

4.1.3.5 Radiative and Auger recombination

Radiative and Auger (band-to-band) recombination are conceivable in SCAPS (4.10). [78]

$$U_{radiative} = k(np + n_i^2) \quad (4.6)$$

$$U_{auger} = (C_n^A n + C_p^A p)(np + n_i^2) \quad (4.7)$$

4.1.3. Interfaces

SCAPS employs thermionic emission for interface transfer. Difference between surrounding layers' thermal velocities affects interface transfer thermal velocity. This model predicts a (small) step in quasi-Fermi level energy levels at an interface, even without band offsets. Like bulk layer recombination canters, interface canters exist. Interface issues are mass faults. Only three types of faults can be multivalent. Pauwels-Vanhoutte hypothesis [79] models' recombination in interface states.

4.2 Device Modeling

The schematic structures of a standard FTO/ GaAs/ FeS₂ and a suggested highly efficient FTO/ GaAs/ FeS₂/CuBi₂O₄ dual heterojunction solar cell are shown in Figures 4.5 and 4.6. FeS₂ has a cubic structure with $a = 5.4195$ as the lattice parameter. This material has a band gap of 0.95 eV and an electron affinity of 4.0 eV. GaAs, on the other hand, has a cubic structure ($a = 5.653$), with a band gap of 1.424 eV and an electron affinity of 4.07 eV. As shown in Figure 4.6, GaAs will form a good p-n junction with FeS₂ with only a few interface flaws that have been considered.

CuBi₂O₄ has a tetragonal structure as well, with lattice values of 5.814 and 5.823, respectively. CuBi₂O₄ has a band gap ranging from 1.4 to 1.8 eV and an electron affinity of 3.73 eV, which is one of its main advantages. CuBi₂O₄ is a back surface field (BSF) for the FeS₂ absorber layer because of its good band alignment, high absorption coefficient, and lattice constant. CuBi₂O₄ almost forms a suitable pp+ junction with FeS₂ layer due to CuBi₂O₄'s E_V shifting upward as a result of the high built-in potential developed at the interface due to higher doping in the BSF layer, leaving a small sharp spike at the interface that can be easily passed by holes, as shown in Figure 4.6. Al and Mo metals with work functions of 4.06 and 4.95 eV were used as cathode and anode, respectively, in the optimized device construction.

The developed FeS₂ based dual heterojunction thin-film solar system is lighted with 100 mW/cm² incident power density under AM1.5G solar spectrum. For the suggested model, the value of the absorption coefficient (cm⁻¹) as a function of wavelength (nm) is chosen from the default configuration in SCAP 1D simulation [78].

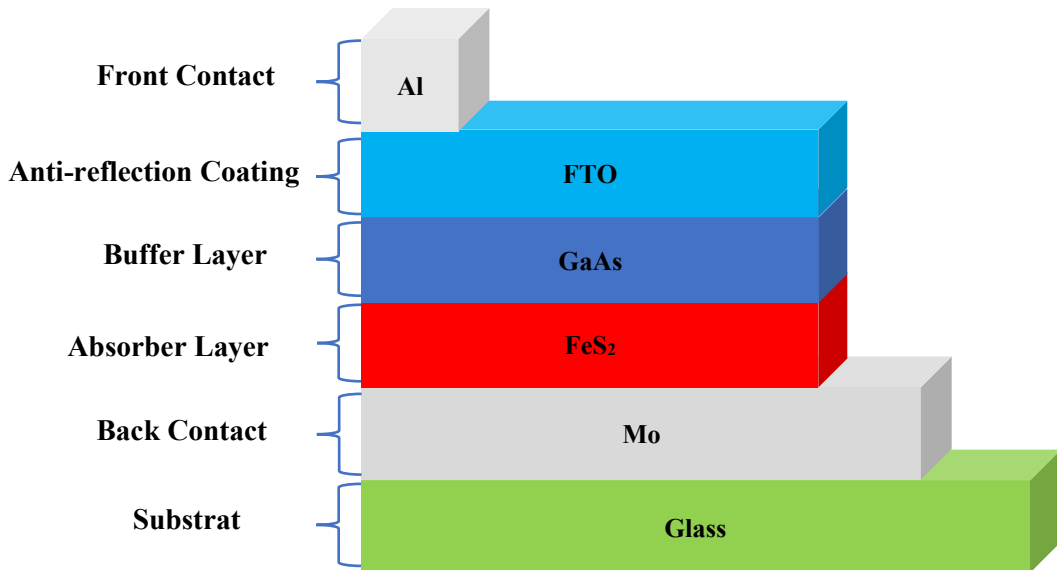


Figure 4.5: Typical Structure of FeS₂ Based Solar Cell.

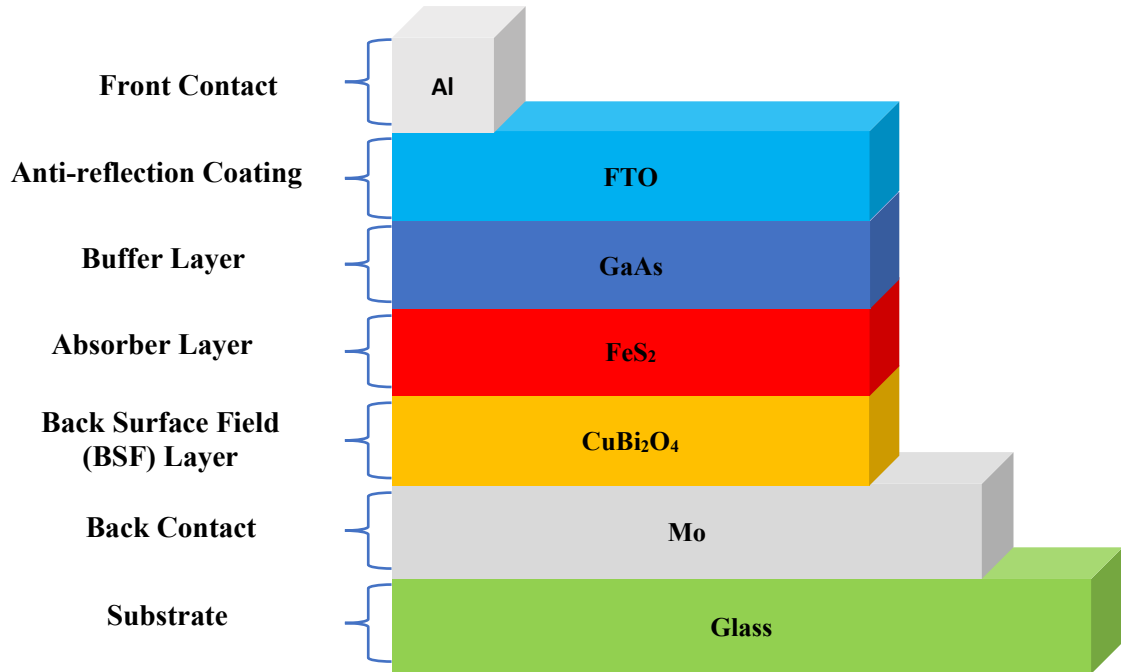


Figure 4.6: Proposed Structure of FeS₂/CuBi₂O₄ Based Dual Heterojunction Solar Cell.

4.3 Design Parameters

Table 4.1, 4.2, and 4.3 indicate the parameters of the n-GaAs/p-FeS₂/p⁺-CuBi₂O₄ solar cell, the interface parameters used in this simulation, and the contact parameters for both the front and back employed in the simulation.

Table 4. 1: Parameters of n-GaAs/p-FeS₂/p⁺-CuBi₂O₄ solar cell.

Parameters	FTO [95]	N GaAs [89]	P FeS ₂ [90-92, 94]	P+ CuBi ₂ O ₄ [80-88, 93]
Layer type	ARC/Window	Buffer	Absorber	BSF
*Thickness [μm]	0.05	0.1	1	0.2
Band gap, E _G [eV]	3.5	1.424	0.95	1.5
Electron affinity, χ [eV]	4	4.07	4.05	3.72
Dielectric permittivity, ε [relative]	9	12.9	10.9	34
Effective CB density, N _C [cm ⁻³]	2.2×10^{18}	4.7×10^{17}	3.0×10^{18}	1.2×10^{19}
Effective VB density, N _V [cm ⁻³]	1.8×10^{19}	9×10^{18}	3.0×10^{19}	5×10^{19}
Electron mobility, μ _n [cm ² V ⁻¹ s ⁻¹]	20	8500	370	1.1×10^{-3}
Hole mobility, μ _p [cm ² V ⁻¹ s ⁻¹]	10	400	70	1.2×10^{-3}
*Donor concentration, N _D [cm ⁻³]	1.0×10^{18}	1.0×10^{17}	0	0
*Acceptor concentration, N _A [cm ⁻³]	0	0	1.0×10^{17}	3.7×10^{18}

Defect type	-	Acceptor	Donor	Donor
Energetic distribution	-	Gaussian	Gaussian	Gaussian
*Peak defect density, $N(t)$ [eV $^{-1}$ cm $^{-3}$]	-	1.0×10^{14}	1.0×10^{12}	1.0×10^{12}
Characteristic energy [eV]	0.1	0.1	0.1	0.1
Reference energy [eV]	0.6	0.6	0.6	0.6
Electron capture cross section for acceptor defect [cm 2]	1.0×10^{-15}	1.0×10^{-15}	1.0×10^{-15}	1.0×10^{-15}
Hole capture cross section for acceptor defect [cm 2]	1.0×10^{-15}	1.0×10^{-15}	1.0×10^{-15}	1.0×10^{-15}
Lattice Constant, a (A)	-	5.653	5.416	5.814

N.B. * are the variable values.

Table 4.2: Parameters of interfaces used in this simulation

Parameters	n-GaAs/p- FeS ₂	p- FeS ₂ /p+- CuBi ₂ O ₄
Defect type	Neutral	Neutral
Capture cross section for electrons [cm $^{-2}$]	10^{-19}	10^{-19}
Capture cross section for holes [cm $^{-2}$]	10^{-19}	10^{-19}
Energetic distribution	Single	Single
Reference for defect energy level E _t	Above the highest E _V	Above the highest E _V
Energy with respect to reference (eV)	0.6	0.6
Total defects (cm $^{-2}$)	10^{10}	10^{10}

Table 4.3: Parameter for Contacts.

Contact	Work Function	Side
Mo	4.36-4.95	Back
Al	4.06-4.26	Front

Chapter 5

Results & Discussion

5.1 Structure Analysis

The solar cell's J-V curve is used to validate the recommended arrangement. When assessing device performance, examine the generation rate, quantum efficiency, and band diagram. The performance parameters V_{OC} , J_{SC} , FF and efficiency are determined by the J-V curve under light through simulation. The basic equation that regulates the features of solar cells is as follows:

$$I = I_{ph} - I_0 \exp\left(\frac{qV}{nk_B T}\right) \quad (5.1)$$

I = net current, I_{ph} = photo-generated current, I_0 = reverse saturation current, V = voltage, n = ideality factor, k_B = Boltzmann constant, and T = Kelvin temperature. Using the J-V curve, we may define I_{ph} as I_{SC} at $V = 0$ V and V as V_{OC} at $I = 0$ A.

$$I_{ph} (\rightarrow I_{SC}) = I_0 \left[\exp\left(\frac{qV_{OC}}{nk_B T}\right) - 1 \right] \quad (5.2)$$

$$V_{OC} \approx \frac{nk_B T}{q} \ln \left[\frac{I_{ph}}{I_0} \right] \quad (5.3)$$

The J-V curves of conventional and FeS₂/CuBi₂O₄ absorber cells is shown in Figure 5.1, with the latter structure clearly showing dominance governed by the V_{OC} . When compared to the standard structure, the bilayer absorber structure shows a significant increase in V_{OC} from 0.517 V to 0.8426 V, a difference of 62.97%. This increase in V_{OC} was achieved by incorporating the CuBi₂O₄ layer, which improved J_{SC} from 46.349 mA/cm² to 49.64 mA/cm² (7.1% improvement) and efficiency from 19.1881% to 33.29% (73.49% improvement). Again, V_{OC} is proportional to the logarithms of photo generated current, I_{ph} in equation (5.3) where I_{ph} is the number of electron-hole pairs created by the absorption process is related. The carrier generation rate in a device is a function of cell distance (x) and can be stated as,

$$G(x) = \int_{\lambda_{min}}^{\lambda_{max}} \alpha(\lambda, x) N_{phot}(\lambda, x) d\lambda \quad (5.4)$$

where, x) and $N_{phot}(\lambda, x)$ are the absorption coefficient and photon flux for each wavelength at each place and λ_{min} and λ_{max} are the short wavelength and long wavelength limits respectively.

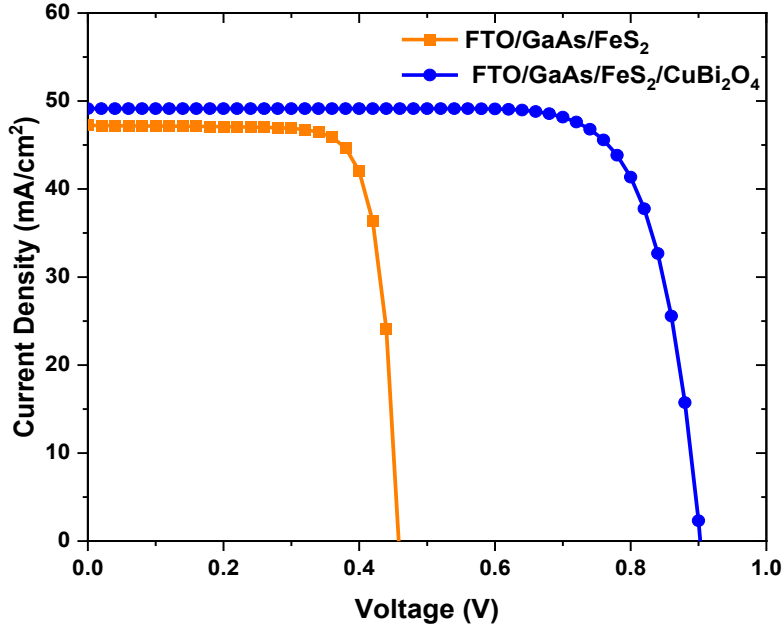


Figure 5.1: J-V characteristics curve of conventional and proposed structure.

In Figure 5.2, the generation rate appears to have increased, indicating the bilayer structure is absorbing light. Thus, the CuBi₂O₄ layer beneath FeS₂ participates in the absorption process, ultimately contributing to the increase of V_{OC} .

The improved generation has no effect on the increase in J_{SC} shown in Figure 5.1 of the bilayer structure. J_{SC} directly depends on Quantum Efficiency, QE , which is the ratio of carriers to incident photons within the active layer of a solar cell.

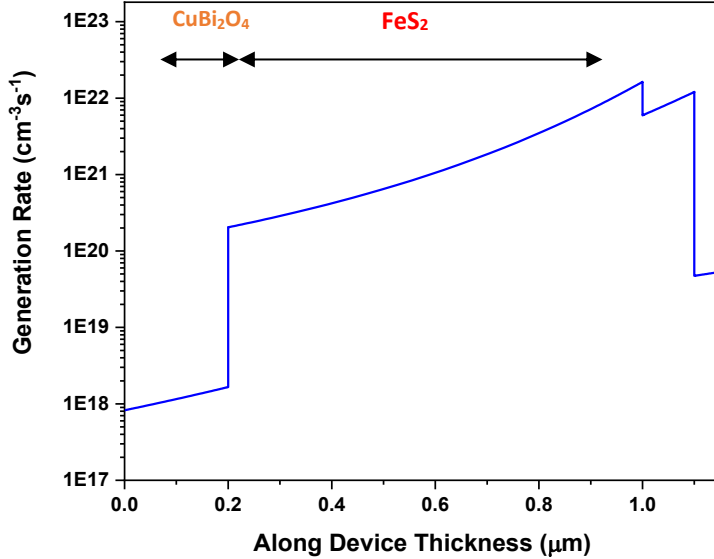


Figure 5.2: Generation rate of the later structure.

In this scenario, QE in turns J_{SC} supports the graph shown in Figure 5.3 in which the two structures have different QE as a function of wavelength.

$$J_{SC} = \frac{q\lambda}{hc} \int S(\lambda) QE(\lambda) d\lambda \quad (5.5)$$

Where, $S(\lambda)$ denotes the intensity of the solar spectrum, and other symbols denote what they say.

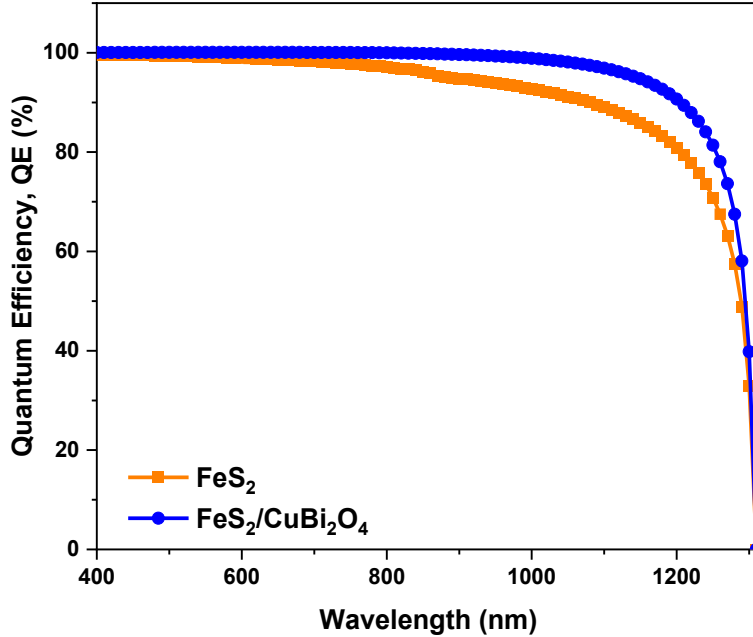


Figure 5.3: Spectral response of typical and bilayer FeS₂/CuBi₂O₄ absorber solar cell.

The band diagram in Figure 5.4 explains the small change in J_{SC} . A FeS₂/CuBi₂O₄ contact has conduction band offset (CBO) and valance band offset (VBO) values of 0.595 eV and 0.045 eV respectively. The VBO generates a barrier for the hole and can backflow from the FeS₂ to CuBi₂O₄ layers.

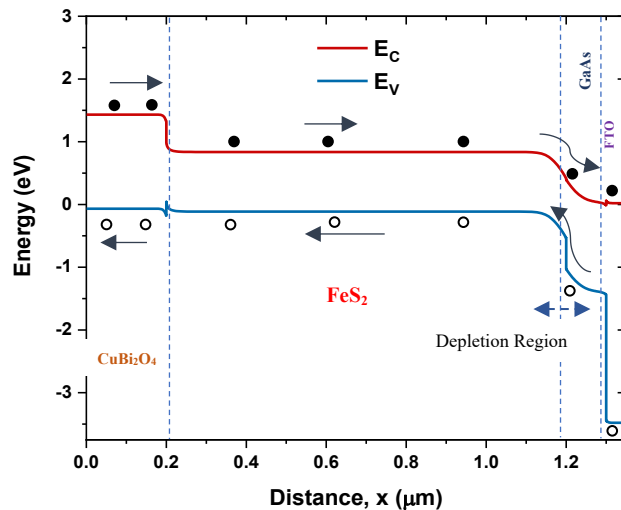


Figure 5.4: Band diagram of FTO/GaAs/FeS₂/CuBi₂O₄ structure.

It may occur due to the band bending downhill as shown in Figure 5.4 affecting the hole mobility. The reverse conveyance of these holes is important in the minor alteration of the current density J_{SC} . The optimized bilayer $\text{FeS}_2/\text{CuBi}_2\text{O}_4$ structure (described later) has acceptor type concentrations of $1.0 \times 10^{17} \text{ cm}^{-3}$ and $3.7 \times 10^{18} \text{ cm}^{-3}$ for FeS_2 and CuBi_2O_4 respectively. The effect of back surface field for FeS_2 and CuBi_2O_4 has occurred for different acceptor concentrations. Other factors may impact the V_{OC} and J_{SC} . For example, a flat band at the $\text{CuBi}_2\text{O}_4/\text{Mo}$ interface leads to good carrier collection when the CuBi_2O_4 layer is doped appropriately.

5.2 Optimization of Proposed Structure

5.2.1 Thicknesses of FeS_2 and CuBi_2O_4 Layers

We initially examined the thicknesses of both absorber layers to improve the suggested solar cell structure of $\text{FeS}_2/\text{CuBi}_2\text{O}_4$ absorber and discover the most acceptable thicknesses for the construction. At the same time, the thickness of FeS_2 layer from 100 to 2000 nm and that of CuBi_2O_4 layer from 100 to 1000 nm is changed to keep doping concentrations at a minimum. $1.0 \times 10^{17} \text{ cm}^{-3}$ (FeS_2) and $3.7 \times 10^{18} \text{ cm}^{-3}$ (CuBi_2O_4) while also ensuring that the total defect density remains constant at 1.01012 cm^{-3} (FeS_2) and $1.0 \times 10^{12} \text{ cm}^{-3}$ (CuBi_2O_4). They are chosen to achieve a compromise between efficiency maximization and overall thin film solar cell thickness.

Figure 5.5 shows that all performance characteristics are almost invariant with CuBi_2O_4 layer thickness for every FeS_2 layer thickness. As shown in Figures 5.5 (a) to 5.5 (d), the CuBi_2O_4 layer contributes little to the overall surplus carrier collection for the solar cell structure. Thus, the thickness of the CuBi_2O_4 layer has no significant effect on the suggested structure's performance. However, increasing the FeS_2 layer thickness improves all PV performance characteristics. Figure 5.5(a) shows that J_{SC} increases from 32.70 mA/cm^2 to 50.45 mA/cm^2 when the thickness increases 100 nm. Increased absorber thickness increases photogeneration, improving I_{ph} and thus J_{SC} , which is directly linked to I_{ph} (5.1). J_{SC} follows the mathematical relationship stated by,

$$J_{SC} = qG(L_p + L_n) \quad (5.6)$$

Where, L_p and L_n are effective electron and hole diffusion length respectively.

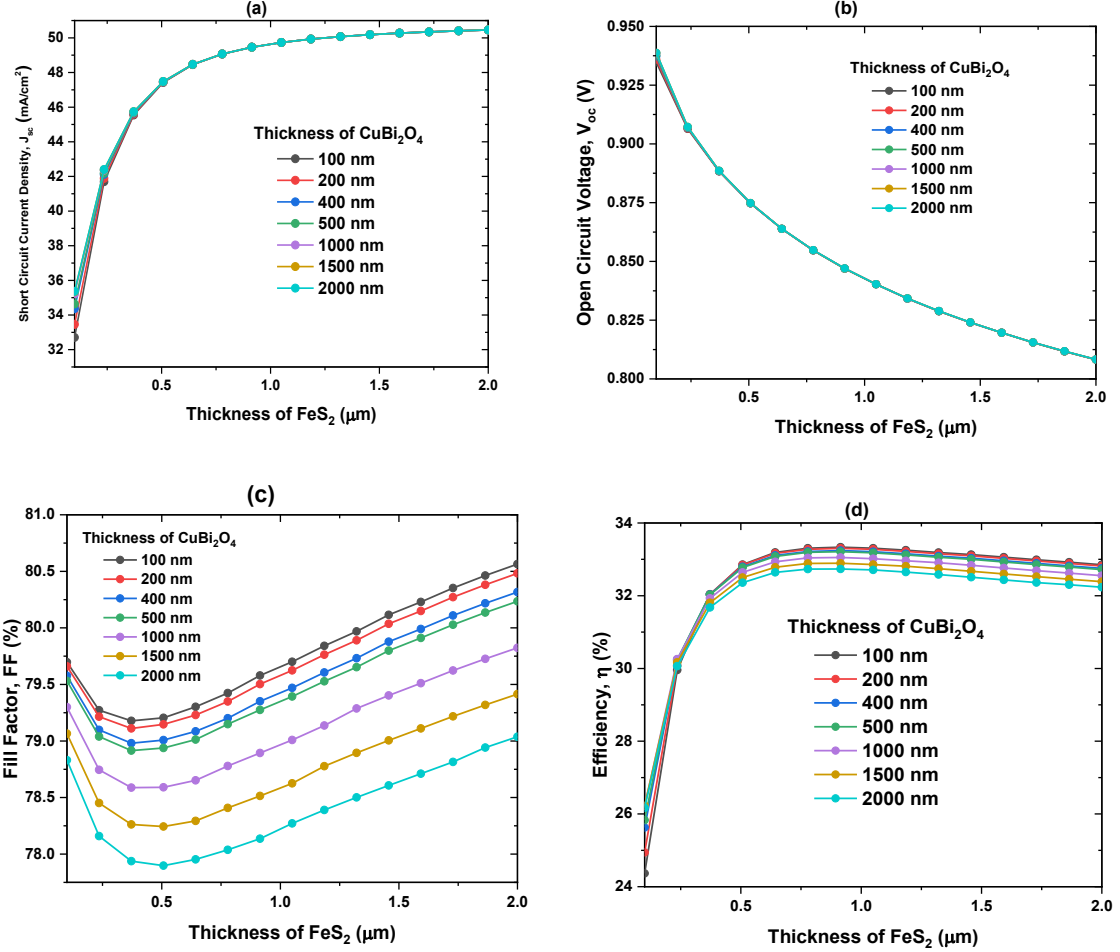


Figure 5.5: Effect on (a) J_{sc} , (b) V_{oc} , (c) FF and (d) η with the variation of Thickness of CuBi₂O₄ for FeS₂ layers.

The capture cross-section and defect density keep both diffusion lengths constant. Thus, the exponential behavior of G dominates the steady growth in J_{sc} with absorber thickness. However, in Figure 5.5(b), as FeS₂ thickness increases from 100 nm to 2000 nm, V_{oc} falls from 0.808 V to 0.933 V. Increased thickness enhances recombination, resulting in more I_0 currents and a minor decrease in V_{oc} in equation (5.3).

As indicated previously, variation in V_{oc} and J_{sc} relates to variance in FF and efficiency, as seen in Figures 5.5 (c) and 5.5 (d). Because FF and V_{oc} are closely related, FF changes at the same pace as V_{oc} . Most importantly, the FeS₂/CuBi₂O₄ bilayer structural efficiency increases from 24.24% at 100 nm FeS₂ to 33.63% at 800 nm FeS₂. Like all other performance factors, efficiency increases slowly with thickness. The efficiency drops from 33.63% to 32.14% when the FeS₂ layer thickness is increased from 800 to 2000 nm. The efficiency of our proposed structure would improve slightly or even fall as the FeS₂ thickness increased. So, we keep the FeS₂ layer at 800 nm thick for our proposed configuration. The CuBi₂O₄ layer is also tuned at 200 nm thickness due to its invariant influence on the solar cell performance with thickness variation. The GaAs buffer layer thickness affects the efficiency of the proposed structure; hence 100 nm is chosen as the thinnest buffer layer available.

Table 5.1: Optimum thickness for proposed structure.

Material	Thickness (μm)
GaAs	0.1
FeS ₂	0.8
CuBi ₂ O ₄	0.2

5.2.2 Doping concentration of FeS₂ Layer

Carrier collection is regulated by absorbing the layer's doping concentration. The layer doping concentrations determine the depletion zone width between layers in a p-n junction solar cell to produce an electric field for photogenerated carriers to move. The depletion width, W , extends to the low doping concentration area according to a thermal equilibrium formulation, implying that,

$$W = \sqrt{\frac{2\epsilon V_{bi}}{q} \left(\frac{N_D + N_A}{N_D N_A} \right)} \quad (5.7)$$

where, V_{bi} is the built-in-potential and other symbols are defined earlier. However, by neglecting the tiny dielectric constant differences between materials, (5.7) can be employed for heterojunctions as well. The depletion area in the primary absorber layer can be adjusted by altering doping concentrations in different locations of a solar cell construction.

To look into the influence of doping concentration on the suggested photovoltaic performance of FeS₂/CuBi₂O₄ structure, we changed the FeS₂ and CuBi₂O₄ p-type concentrations. The doping concentration of FeS₂ is changed from 10^{15} cm^{-3} to 10^{17} cm^{-3} . CuBi₂O₄ p-type concentrations are chosen from $3.7 \times 10^{16} \text{ cm}^{-3}$ to $3.7 \times 10^{20} \text{ cm}^{-3}$. Table 4.1 shows the n-type doping concentrations of FTO and GaAs.

Figure 5.6(a) demonstrates that for all CuBi₂O₄ doping levels, short circuit current density J_{SC} increases with FeS₂ layer doping concentration but remains constant for CuBi₂O₄ doping density at 3.7×10^{19} to $3.7 \times 10^{20} \text{ cm}^{-3}$. Figure 5.6 (b) shows that for both FeS₂ and CuBi₂O₄, open circuit voltage, V_{OC} remains constant with doping density. The doping density of CuBi₂O₄ increased from $3.7 \times 10^{16} \text{ cm}^{-3}$ to $3.7 \times 10^{20} \text{ cm}^{-3}$, resulting in only minor variations in 0.841V.

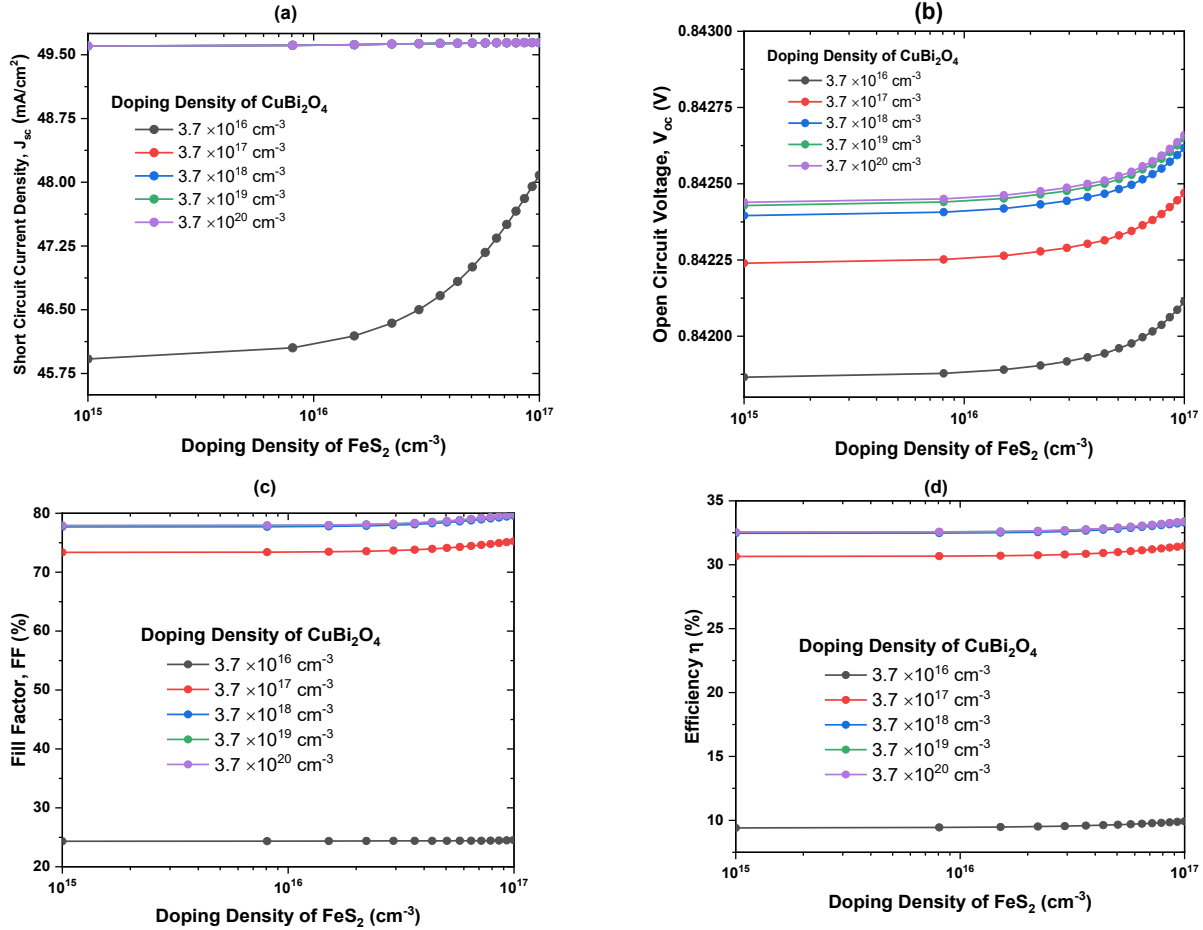


Figure 5.6: Effect on (a) J_{sc} , (b) V_{oc} , (c) FF and (d) η with the variation of Doping Concentration of CuBi₂O₄ for FeS₂ layers.

The FF increases with CuBi₂O₄ doping concentration, peaking at $3.7 \times 10^{20} \text{ cm}^{-3}$ doping level layer. The efficiency of the bilayer structure follows a similar pattern. Efficiency changes from 10% to 33% with increasing CuBi₂O₄ doping density but is essentially invariant with FeS₂ doping density. The increase in CuBi₂O₄ doping density intensifies the electric field, increasing device efficiency. Our proposed best optimal efficiency FeS₂/CuBi₂O₄ bilayer structure is found to be 33.29% for FeS₂ and CuBi₂O₄ doping concentrations at 10^{19} cm^{-3} and $3.7 \times 10^{18} \text{ cm}^{-3}$ respectively with $V_{OC} = 0.842 \text{ V}$, $J_{SC} = 49.64 \text{ mA/cm}^2$ and FF = 79.58%.

5.2.3 Doping concentrations of CuBi₂O₄ layer

So, we could see the effect of CuBi₂O₄ layer more clearly, we changed the doping concentration of CuBi₂O₄ layer from 10^{16} cm^{-3} (very lightly doped, p-) to 10^{20} cm^{-3} (heavily doped, p+). Figure 5.7 summarizes the photovoltaic performance effects. When stated previously, all performance measures improve as the CuBi₂O₄ layer's doping concentration increases. As the CuBi₂O₄ layer doping concentration increases, the depletion zone at the FeS₂/CuBi₂O₄ interface moves closer to the FeS₂, as seen in Figure 5.7. while the FeS₂/CuBi₂O₄ contact remains constant for a given FeS₂ concentration. This enhances carrier collection at the FeS₂/CuBi₂O₄ contact and thus performance. The benefit is more obvious at lower FeS₂ doping levels, while it saturates at higher FeS₂ doping levels.

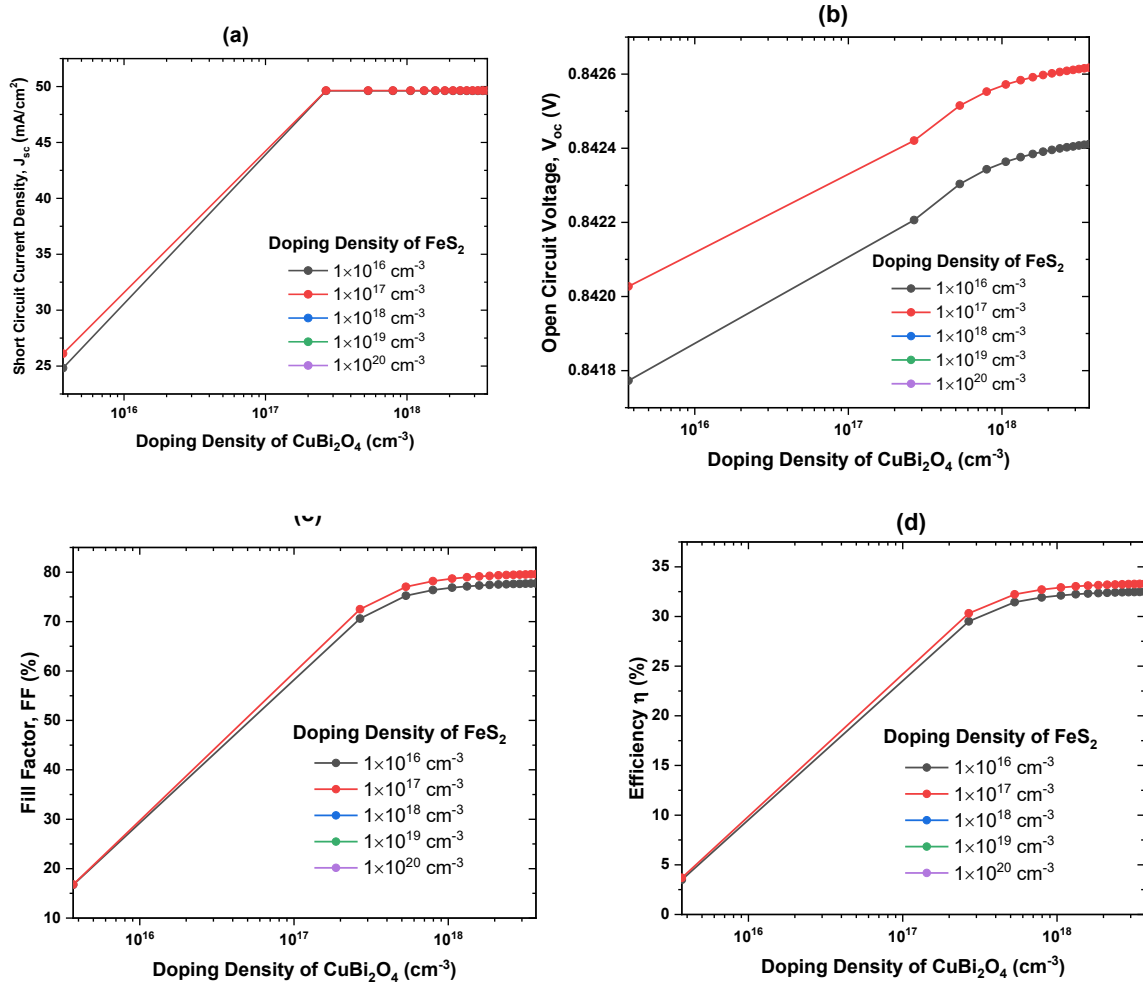


Figure 5.7: Effect on (a) J_{sc} , (b) V_{oc} , (c) FF and (d) η with the variation of Doping Concentration of FeS_2 for CuBi_2O_4 layers.

$\text{FeS}_2/\text{CuBi}_2\text{O}_4$ structure can greatly improve solar cell performance by keeping the CuBi_2O_4 layer doped at a high but usable level for each material, Table 5.2 indicates the optimal doping density.

Table 5.2: Optimum Doping Profile for Proposed Structure.

Material	Donor Doping Density (cm^{-3})	Acceptor Doping Density (cm^{-3})
GaAs	10^{18}	0
FeS_2	0	10^{17}
CuBi_2O_4	0	3.7×10^{18}

5.2.4 Bulk Defect Density

Bulk defect states can operate as recombination hotspots for photogenerated carriers, affecting photovoltaic cell performance. We add neutral defects into the bilayer structure to measure the influence of absorber layer defect states on photovoltaic cell performance with defect state density ranging from 10^{15} cm^{-3} to 10^{20} cm^{-3} in FeS_2 and CuBi_2O_4 absorber layers respectively.

Figure 5.8 shows V_{OC} , J_{SC} , FF, and varying with defect state density. All cell metrics decrease with increasing defect state density in the FeS_2 layer, regardless of the $CuBi_2O_4$ layer. For a bulk FeS_2 layer with a defect state density of $10^{20} cm^{-3}$, the efficiency practically equals zero. To improve cell performance, the density of defective states in bulk FeS_2 must be reduced to a minimum. Because there is no substantial change in $CuBi_2O_4$ defect state density, all lines illustrating different levels of $CuBi_2O_4$ defect state density are overlapped in Figure 5.8.

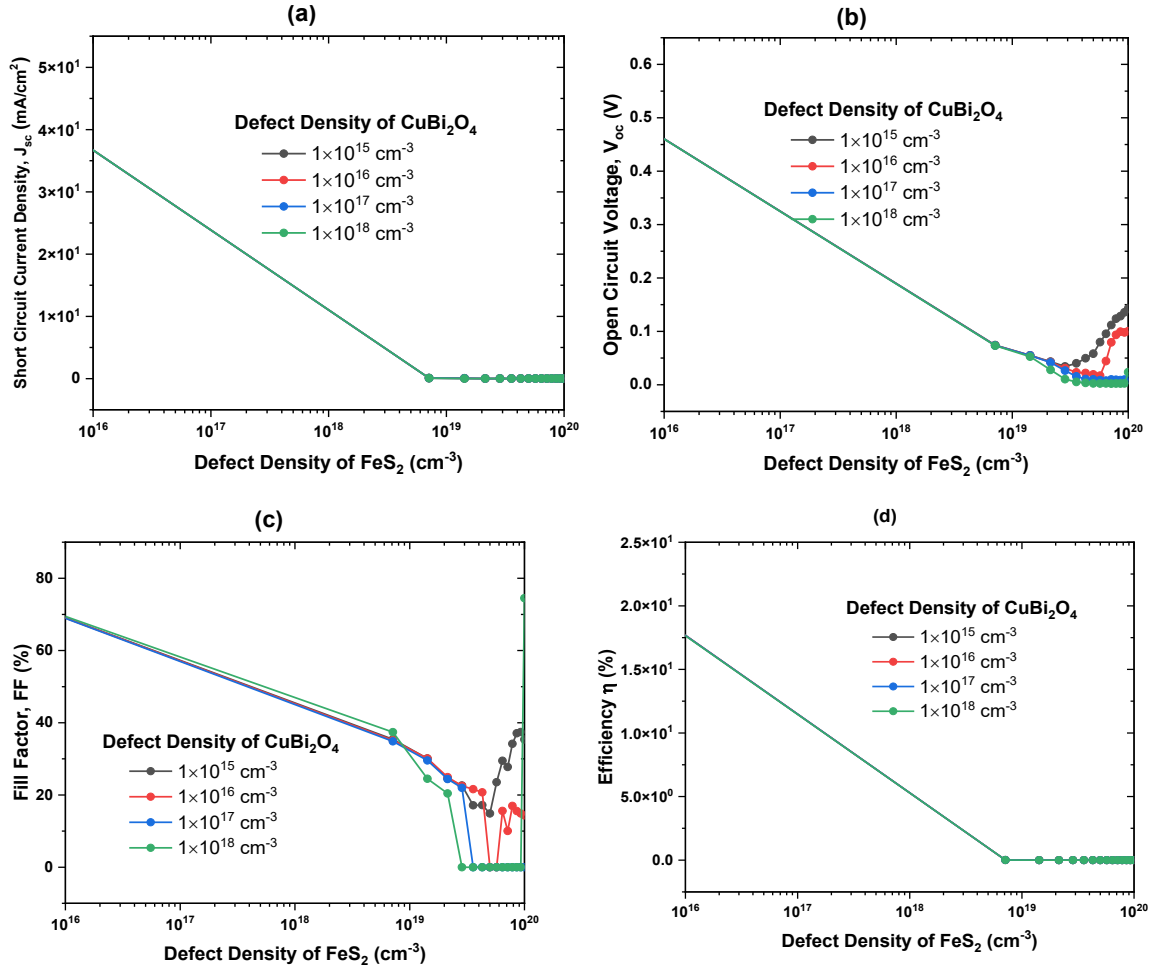


Figure 5.8: Effect on (a) J_{SC} , (b) V_{OC} , (c) FF and (d) η with the variation of Defect Level Density of $CuBi_2O_4$ for FeS_2 layers.

5.3 The Effects of Series and Shunt Resistance

The series (R_S) and shunt (R_{SH}) resistances have a significant impact on the solar cell's performance. Contacts between the device's layers, anode and cathode metal contacts, and manufacturing faults all contribute to these resistances.

For resistance of the series, the fill factor (FF) of the devices is affected. When the solar cell has a lower R_S and a higher R_{SH} , it achieves greater power conversion efficiency (PCE). The effect of series and shunt resistances on the PV performance of the proposed solar cell construction is shown in Figures 5.9 to 5.10.

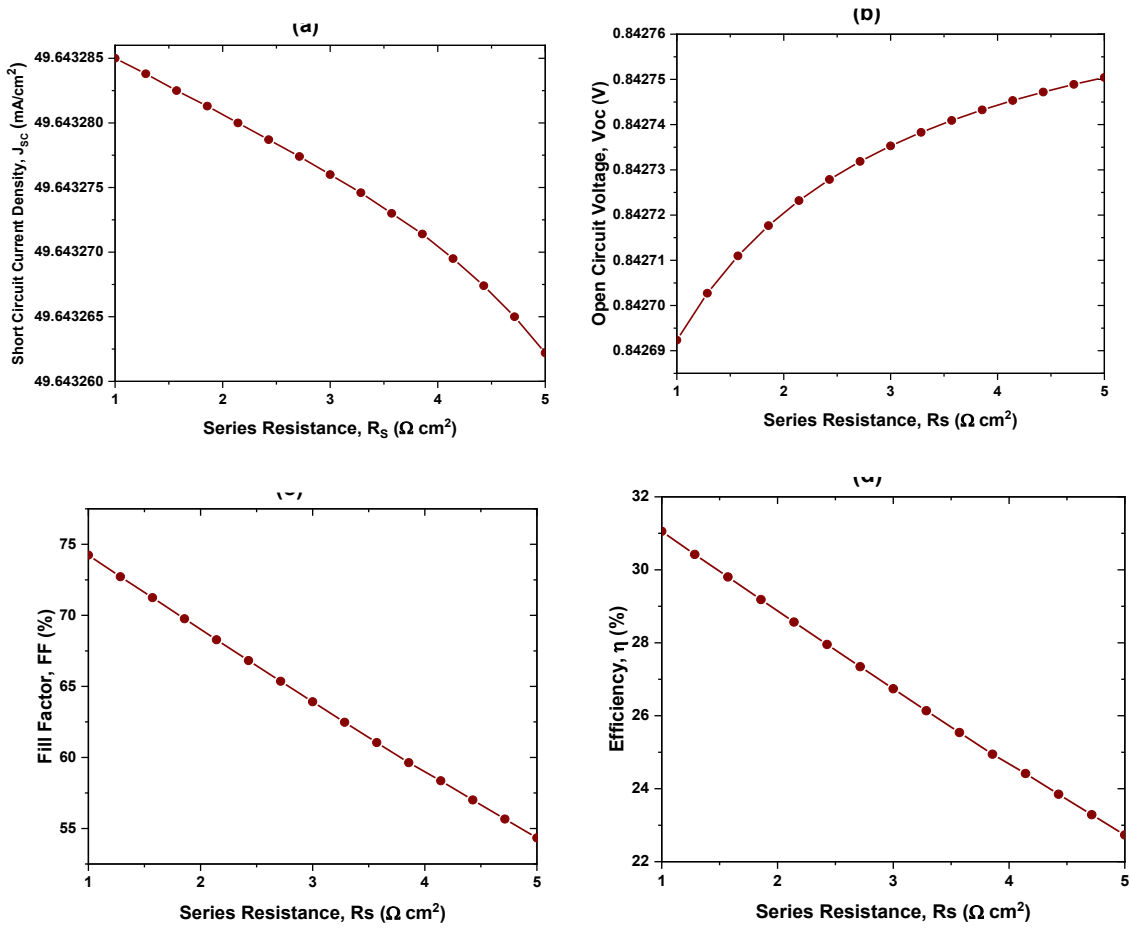
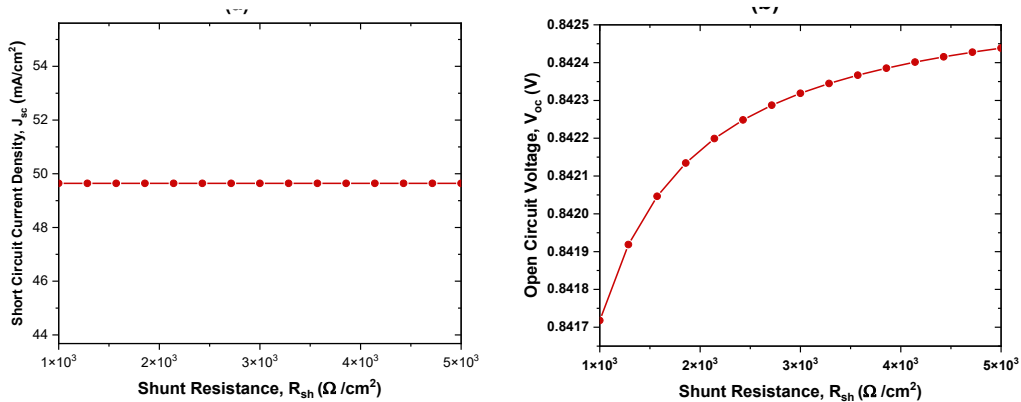


Figure 5.9: Effect on (a) J_{SC} , (b) V_{OC} , (c) FF and (d) η with the variation of Series Resistance.

Figure 5.9(c) indicates that when the R_S increases from 1 to $5 \Omega\text{cm}^2$, the FF of the solar cell drops. The V_{OC} and J_{SC} both changed as the R_S changed. The drop in FF of the solar cell causes the PCE to decrease. For a change in R_S from 1 to $5 \Omega\text{cm}^2$, the PCE drops from 33.7% to 24.36%.

Figure 5.10 depicts the change in PV characteristics as a function of device shunt resistance. The R_{SH} has ranged between 1 and $5 \text{ k}\Omega\text{cm}^2$. Only J_{SC} is independent of R_{SH} , as can be seen in the diagram. With increased R_{SH} , V_{OC} , FF and efficiency all rise.



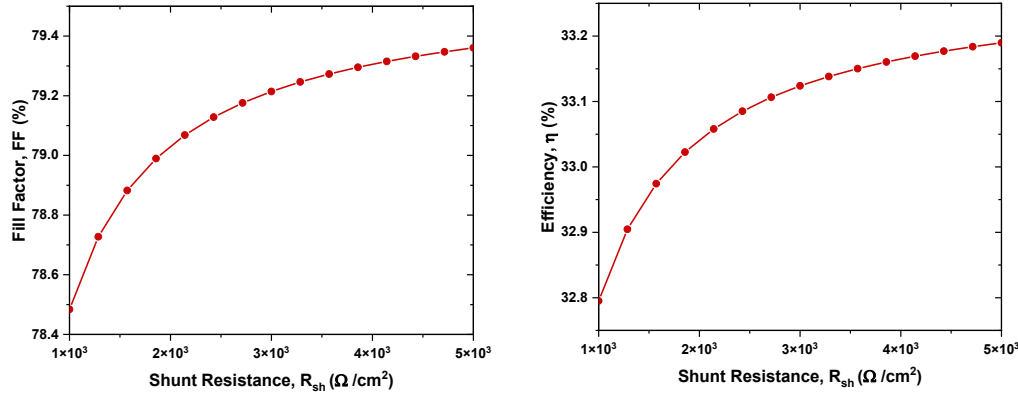


Figure 5.10: Effect on (a) J_{sc} , (b) V_{oc} , (c) FF and (d) η with the variation of Shunt Resistance.

5.4 The Effects of Temperature

The temperature affects the performance of solar cells. Temperature enhances charge carrier velocity in semiconductors, reducing bond energy. This lower bond energy reduces the semiconductor's band gap, affecting intrinsic carrier concentrations. The increase in intrinsic carriers raises the solar cell's saturation current.

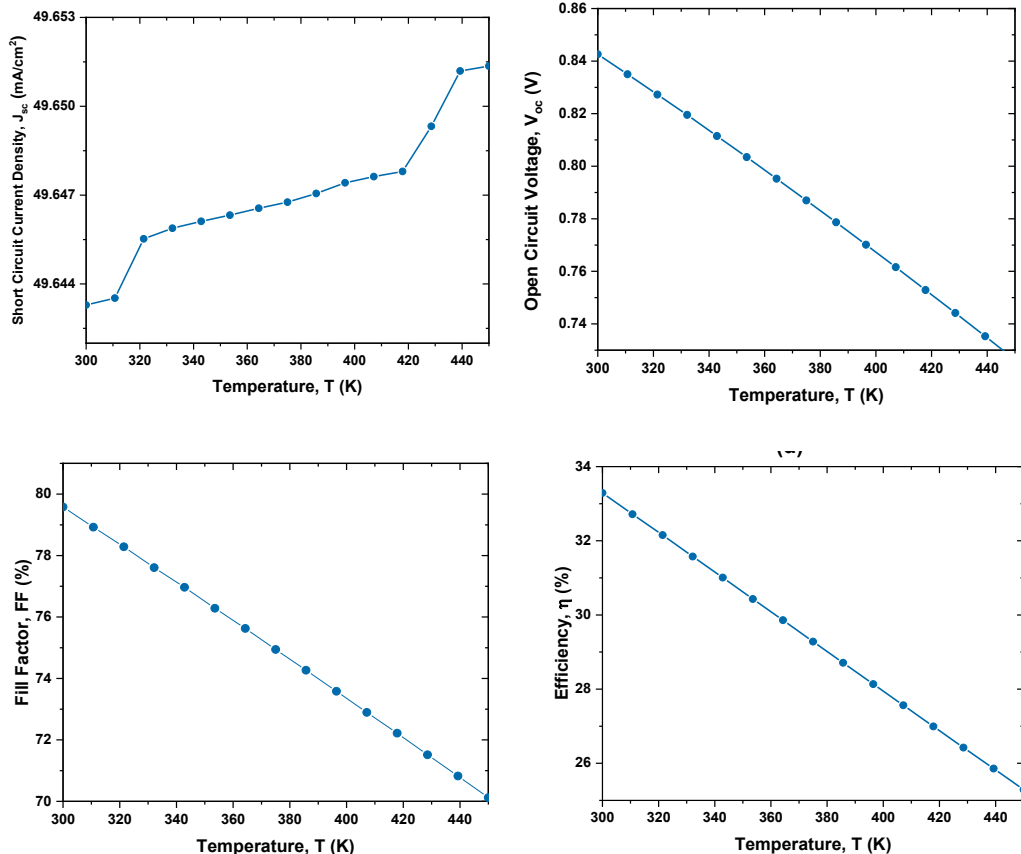


Figure 5.11: Influence on (a) J_{sc} , (b) V_{oc} , (c) FF and (d) η with the variation of Temperature.

As shown in Figure 5.12, the suggested solar cell performs best between 300 and 450 K. The short circuit current of a solar cell is generally temperature independent, as seen in the diagram. The solar cell's V_{OC} reduces dramatically as the temperature rises, which is owing to the solar cell's reverse saturation current increasing with temperature. FF, on the other hand, varies greatly with temperature. As the V_{OC} of the solar cell falls, the PCE of the solar cell decreases. At greater temperatures, the collision between photocarriers and vibrating atoms increases, potentially resulting in power loss in the solar cell.

5.5 Optimized Cell Performance of FeS₂ Based Structure

Figure 5.13 shows the J-V characteristics of FTO/GaAs/FeS₂ and FTO/GaAs/FeS₂/CuBi₂O₄ solar cell respectively. Table 5.3 shows the device performance of the optimized solar cells.

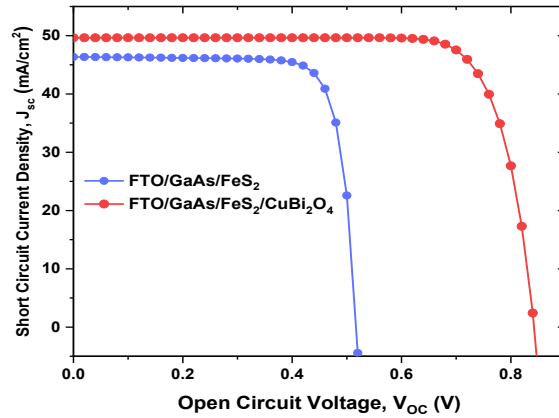


Figure 5.12: J-V Characteristics for optimal structure.

The increased efficiency of solar cell is owing to increased built-in potential and decreased saturation current. The CuBi₂O₄ BSF layer boosts the solar cell's J_{SC} significantly. Thus, significant rise in J_{SC} is due to longer wavelength, sub-band gap photon absorption in the BSF layer.

Table 5.3: Device performance of the optimized FeS₂ based solar cells.

Parameters	FeS ₂ Absorber Layer	FeS ₂ /CuBi ₂ O ₄ Absorber Layer
Short Circuit Current Density, J_{sc} (mA/cm ²)	46.349	49.64
Open Circuit Voltage, V_{oc} (V)	0.517	0.8426
Fill Factor, FF (%)	80.0242	79.58
Efficiency, η (%)	19.1881	33.29
Max. Voltage, V_{mpp} (V)	0.442	0.703
Max. Current, J_{mpp} (mA/cm ²)	13.391	47.355

Figure 5.3 compares the QE of FTO/GaAs/FeS₂ and FTO/GaAs/FeS₂/CuBi₂O₄ solar cells. As seen in Figure 5.3, the CuBi₂O₄ BSF layer significantly changes the QE of the solar cell. Because of the tail states in the CuBi₂O₄ BSF layer, the suggested solar cell's QE marginally increases from 800 to 1300 nm, increasing the J_{SC} . Table 5.4 compares CdTe, CIGS, Ge, GaAs, FeS₂ and perovskite etc. thin film solar cells.

Table 5.4: Performance of the proposed solar cell in comparison with other solar cells.

No.	Thin Film Solar Cell	V_{oc} (V)	J_{sc} (mA/cm ²)	FF (%)	PCE (%)	Type	Reference
1.	a-Si	0.859	17.5	63	9.5	Experimental	[96]
2.	Si (crystalline)	0.705	42.7	82.8	25.0	Experimental	[97]
3.	Si (multi-crystalline)	0.664	37.7	78.9	20.3	Experimental	[96]
4.	CIGS	0.734	39.58	80.40	23.84	Experimental	[98]
5.	Perovskite	1.18	25.14	84.8	25.20	Experimental	[99]
6.	CdTe	0.887	31.69	78.50	22.10	Experimental	[100]
7.	GaAs	1.127	29.78	86.70	29.10	Experimental	[99]
8.	CZTS	0.716	33.7	80.3	19.4	Experimental	[96]
9.	FeS ₂	0.842	49.64	79.59	33.29	Theory	Proposed

Table 5.4 shows that a FeS₂ based dual-heterojunction solar cell with a predicted efficiency of 33.29 % has the potential to harvest solar energy soon.

Chapter 6

Conclusion & Future Work

6.1 Conclusion

In this project SCAPS 1D simulator was used to create and simulate a novel FeS₂ based dual heterojunction solar cell. As a buffer and BSF layer the GaAs and CuBi₂O₄ materials were used respectively. Each layer's thickness, doping, and defect density have all been tuned for this device. The proposed structure optimized and efficiency was found to be from 19.19 % to 33.29 % which was an increment of 73.493%. This increment had happened for the incorporation of BSF layer of CuBi₂O₄.The solar cell had a higher short circuit current density, J_{SC} of 49.69 mA/cm² which is appropriate for FeS₂ martial with a low band gap. The higher built-in potentials developed at the n-GaAs/p-FeS₂ and p-FeS₂/p+ CuBi₂O₄ interfaces due to suitable band alignment give the dual heterojunction solar cell a higher open circuit voltage, V_{OC} of 0.8426V.

In real life fabrication, various defects- interface defects, surface recombination, scattering etc. will minimize efficiency. However, if 70-80% of simulated efficiency can be found that will be a breakthrough for making low-cost thin film solar cell. So, this numerical analysis shows that a FeS₂ based thin film solar cell has the potential to be commercialized in the near future because of its high efficiency.

6.2 Future Work

The study of thin-film solar cells is continuing and there are still many questions to be answered. Various varieties of high-efficiency industry-standard solar cells have been manufactured; however, they are restricted to a single high-end application. The goal of our work is to increase solar cell efficiency along with bringing down the cost of solar cell and make it available for everyone, especially in third-world countries.

FeS₂ has been already proven as a promising candidate for the next generation ultrathin solar cell. The main challenge is to fabricate pure FeS₂ crystal with the minimum defects. Another challenge is to make the layer structure of FeS₂ with other materials which have been simulated for the first time incorporating CuBi₂O₄ as BSF layer in this project. There are still very few work that has been done in FeS₂ based solar cell. So, in short, the future work considering this material is:

- Fabricating the proposed model in the Laboratory.
- Fabricating moderately pure FeS₂ crystal.
- Incorporating different material with suitable band alignment as BSF layer.
- Incorporating FeS₂ in layers structure with other different materials.
- Testing FeS₂ in P-I-N structure which is unexplored.
- Doping FeS₂ as an n-type material is also a good choice for future experiments.
- Alternating the front side (p type/n type) of the solar cell where the photon is captured.

- Varying dopant density and observing the change of properties of FeS_2 in a laboratory.

As the FeS_2 small bandgap imposes an efficiency-limiting of V_{OC} pyrite could be alloyed so its energy gap rises while maintaining the high absorption coefficient and reasonably high mobility of free carriers. This could be alternative way to increase V_{OC} thus also increasing the FeS_2 based solar cell power conversion efficiency.

Reference

- [1] J. P. Dorian, H. T. Franssen, and D. R. Simbeck, "Global challenges in energy," *Energy Policy*, vol. 34, no. 15, pp. 1984–1991, 2006.
- [2] "The biggest energy challenges facing humanity," BBC News, Mar. 13, 2017. [Online]. Available: <https://www.bbc.com/future/article/20170313-the-biggest-energy-challenges-facing-humanity> [Accessed: Apr. 30, 2022].
- [3] "Annual change in solar energy generation," Our World in Data, 2019. [Online]. Available: <https://ourworldindata.org/grapher/annual-change-solar?time=2019> [Accessed: Apr. 30, 2022].
- [4] K. S. Deffeyes, *Hubbert's Peak: The Impending World Oil Shortage*, New ed. Princeton, NJ, USA: Princeton Univ. Press, 2008.
- [5] "Statistical Review of World Energy," BP, 2003. [Online]. Available: <https://www.bp.com/en/global/corporate/energy-economics/statistical-review-of-worldenergy.html> [Accessed: Apr. 30, 2022].
- [6] "Price Data—HEPI," HEPI, 2021. [Online]. Available: <https://www.energypriceindex.com/latest-update> [Accessed: Apr. 30, 2022].
- [7] "Electricity generation," Wikipedia. [Online]. Available: https://en.wikipedia.org/wiki/Electricity_generation [Accessed: Apr. 30, 2022].
- [8] "Renewable energy explained," U.S. Energy Information Administration (EIA), Jun. 1, 2021. [Online]. Available: <https://www.eia.gov/energyexplained/renewable-sources/> [Accessed: Apr. 30, 2022].
- [9] "Asia's growing renewable energy capacity is a bullish sign for investors," Energy Tracker Asia. [Online]. Available: <https://energytracker.asia/asias-growing-renewable-energy-capacity-is-a-bullish-sign-for-investors/> [Accessed: Apr. 30, 2022].
- [10] R. J. Komp, *Practical Photovoltaics: Electricity from Solar Cells*, 3rd ed. Aatec Publications, 1990.
- [11] D. E. Carlson and C. R. Wronski, "Amorphous silicon solar cell," *Appl. Phys. Lett.*, vol. 28, no. 11, pp. 671–673, 1976.
- [12] J. Perlin, *From Space to Earth: The Story of Solar Electricity*. Aatec Publications, 1999.
- [13] D. M. Chapin, C. S. Fuller, and G. L. Pearson, "A new silicon p-n junction photocell for converting solar radiation into electrical power," *J. Appl. Phys.*, vol. 25, no. 5, pp. 676–677, 1954.
- [14] H. C. Card and E. S. Yang, "Electronic processes at grain boundaries in polycrystalline semiconductors under optical illumination," *IEEE Trans. Electron Devices*, vol. 24, no. 4, pp. 397–402, 1977.

- [15] R. J. Komp, *Practical Photovoltaics: Electricity from Solar Cells*, 3rd ed. Aatec Publications, 1990.
- [16] F. Baig et al., "Numerical analysis a guide to improve the efficiency of experimentally designed solar cell," *Appl. Phys. A*, vol. 124, p. 471, 2018. doi: 10.1007/s00339-018-1877-x.
- [17] F. Baig et al., "Mitigation of interface recombination by careful selection of ETL for efficiency enhancement of MASnI₃ solar cell," *Optik*, vol. 170, pp. 463–474, 2018. doi: 10.1016/j.ijleo.2018.05.135.
- [18] F. Baig et al., "Efficiency enhancement of CH₃NH₃SnI₃ solar cells by device modeling," *J. Electron. Mater.*, vol. 47, pp. 5275–5282, 2018. doi: 10.1007/s11664-018-6406-3.
- [19] F. Baig, H. Ullah, Y. H. Khattak, and B. M. Soucase, "Numerical analysis of SnS photovoltaic cells," in *Proc. Int. Renew. Sustain. Energy Conf. (IRSEC)*, 2016, pp. 596–600. doi: 10.1109/IRSEC.2016.7983899.
- [20] F. Baig et al., "Efficiency enhancement of SnS solar cell using back surface field," in *Proc. 1st Int. Conf. Power, Energy Smart Grid (ICPESG)*, 2018, pp. 1–5. doi: 10.1109/ICPESG.2018.8384496.
- [21] Y. H. Khattak et al., "Enhancement of the conversion efficiency of thin film kesterite solar cell," *J. Renew. Sustain. Energy*, vol. 10, no. 3, p. 033501, 2018. doi: 10.1063/1.5023478.
- [22] Y. H. Khattak et al., "Effect of CZTSe BSF and minority carrier life time on the efficiency enhancement of CZTS kesterite solar cell," *Curr. Appl. Phys.*, vol. 18, pp. 633–641, 2018. doi: 10.1016/j.cap.2018.03.013.
- [23] Y. H. Khattak et al., "Numerical modeling baseline for high efficiency (Cu₂FeSnS₄) CFTS based thin film kesterite solar cell," *Optik*, vol. 164, pp. 547–555, 2018. doi: 10.1016/j.ijleo.2018.03.055.
- [24] A. Ennaoui et al., "Iron disulfide for solar energy conversion," *Sol. Energy Mater. Sol. Cells*, vol. 29, pp. 289–370, 1993.
- [25] M. Limpinsel et al., "An inversion layer at the surface of n-type iron pyrite," *Energy Environ. Sci.*, vol. 7, p. 1974, 2014.
- [26] M. Cabán-Acevedo et al., "Ionization of high-density deep donor defect states explains the low photovoltage of iron pyrite single crystals," *J. Am. Chem. Soc.*, vol. 136, pp. 17163–17179, 2014.
- [27] S. Shukla et al., "Origin of photocarrier losses in iron pyrite (FeS₂) nanocubes," *ACS Nano*, vol. 10, pp. 4431–4440, 2016.
- [28] A. Hosen, M. Mian, and S. R. A. Ahmed, "Simulating the performance of a highly efficient CuBi₂O₄-based thin-film solar cell," *SN Appl. Sci.*, vol. 3, no. 5, pp. 1–13, 2021.
- [29] E. Becquerel, "Mémoire sur les effets électriques produits sous l'influence des rayons solaires," *Comptes Rendus*, vol. 9, pp. 561–567, 1839.

- [30] A. Einstein, "Über einen die Erzeugung und Verwandlung des Lichtes betreffenden heuristischen Gesichtspunkt," *Annalen der Physik*, vol. 17, pp. 132–148, 1905.
- [31] U. Malm, "Modelling and degradation characteristics of thin-film CIGS solar cells," Ph.D. dissertation, Dept. Eng. Sci., Uppsala Univ., Uppsala, Sweden, 2008.
- [32] A. Smets, K. Jager, O. Isabella, and R. van Swaaij, *Solar Energy: The Physics and Engineering of Photovoltaic Conversion, Technologies and Systems*. Cambridge, UK: UIT Cambridge, 2016.
- [33] F. Kasten and A. T. Young, "Revised optical air mass tables and approximation formula," *Appl. Opt.*, vol. 28, pp. 4735–4738, 1989.
- [34] B. Zeghbroueck, "Principles of Semiconductor Devices," 2011. [Online]. Available: <https://www.academia.edu/37995678> [Accessed: Apr. 30, 2022].
- [35] A. Marzo, F. Beiza, P. Ferrada, J. Alonso, and R. Roman, "Comparison of Atacama Desert solar spectrum vs. ASTM G173-03 reference spectra for solar energy applications," presented at the EuroSun 2016, 2016. doi: 10.18086/eurosun.2016.09.01.
- [36] W. Shockley and H. J. Queisser, "Detailed balance limit of efficiency of p-n junction solar cells," *J. Appl. Phys.*, vol. 32, pp. 510–519, 1961.
- [37] M. A. Green, *Solar Cells*. Englewood Cliffs, NJ, USA: Prentice-Hall, 1982.
- [38] A. M. Bagher, M. M. A. Vahid, and M. Mohsen, "Types of solar cells and application," *Am. J. Opt. Photonics*, vol. 3, no. 5, pp. 94–113, 2015.
- [39] "Department of Energy & Climate Change," GOV.UK, 2017. [Online]. Available: <https://www.gov.uk/government/organisations/department-of-energy-climate-change> [Accessed: Apr. 30, 2022].
- [40] A. Polizzotti et al., "The state and future prospects of kesterite photovoltaics," *Energy Environ. Sci.*, vol. 6, pp. 3171–3182, 2013.
- [41] "FeS₂ (Pyrite)," PVEducation. [Online]. Available: <https://www.pveducation.org/pvcdrom/materials/fes2-pyrite> [Accessed: Apr. 30, 2022].
- [42] J. A. Wilson and A. D. Yoffe, "The transition metal dichalcogenides discussion and interpretation of the observed optical, electrical and structural properties," *Adv. Phys.*, vol. 18, no. 73, pp. 193–335, 1969.
- [43] G. Sharma et al., "Electronic structure, photovoltage, and photocatalytic hydrogen evolution with p-CuBi₂O₄ nanocrystals," *J. Mater. Chem. A*, vol. 4, no. 8, pp. 2936–2942, 2016.
- [44] S. P. Berglund et al., "Comprehensive evaluation of CuBi₂O₄ as a photocathode material for photoelectrochemical water splitting," *Chem. Mater.*, vol. 28, no. 12, pp. 4231–4242, 2016.

- [45] N. T. Hahn, V. C. Holmberg, B. A. Korgel, and C. B. Mullins, "Electrochemical synthesis and characterization of p-CuBi₂O₄ thin film photocathodes," *J. Phys. Chem. C*, vol. 116, no. 10, pp. 6459–6466, 2012.
- [46] F. Wang et al., "Gradient self-doped CuBi₂O₄ with highly improved charge separation efficiency," *J. Am. Chem. Soc.*, vol. 139, no. 42, pp. 15094–15103, 2017.
- [47] J. Fink et al., "The electronic structure of high-T_c superconductors," in *High-T_c Superconductors and Related Materials*, Dordrecht: Springer, 2001, pp. 1–38.
- [48] O. Janson, R. O. Kuzian, S. L. Drechsler, and H. Rosner, "Electronic structure and magnetic properties of the spin-1/2 Heisenberg magnet Bi₂CuO₄," *Phys. Rev. B*, vol. 76, no. 11, p. 115119, 2007.
- [49] D. Di Sante et al., "Realizing double Dirac particles in the presence of electronic interactions," *Phys. Rev. B*, vol. 96, no. 12, p. 121106, 2017.
- [50] Z. X. Shen et al., "Photoemission study of CuO and Cu₂O single crystals," *Phys. Rev. B*, vol. 42, no. 13, pp. 8081–8085, 1990.
- [51] D. D. Sarma and K. Sreedhar, "Electronic structure of square planar CuO₄ 6- clusters," *Z. Phys. B*, vol. 69, no. 4, pp. 529–534, 1988.
- [52] M. R. Brozel and G. E. Stillman, *Properties of Gallium Arsenide*, 3rd ed. London, UK: INSPEC, 1996.
- [53] A. Gomes et al., "Voltammetric study of the Fe-S-Ebonex system," *J. Appl. Electrochem.*, vol. 25, no. 11, pp. 1045–1051, 1995.
- [54] R. Schieck et al., "Electrical properties of natural and synthetic pyrite (FeS₂) crystals," *J. Mater. Res.*, vol. 5, no. 7, pp. 1567–1572, 1990.
- [55] B. Voigt et al., "Transport evidence for sulfur vacancies as the origin of unintentional n-type doping in pyrite FeS₂," *ACS Appl. Mater. Interfaces*, vol. 11, no. 17, pp. 15552–15563, 2019.
- [56] C. Wadia, A. P. Alivisatos, and D. M. Kammen, "Materials availability expands the opportunity for large-scale photovoltaics deployment," *Environ. Sci. Technol.*, vol. 43, no. 6, pp. 2072–2077, 2009.
- [57] P. P. Altermatt et al., "Specifying targets of future research in photovoltaic devices containing pyrite (FeS₂) by numerical modelling," *Sol. Energy Mater. Sol. Cells*, vol. 71, no. 2, pp. 181–195, 2002.
- [58] I. Sullivan, B. Zoellner, and P. A. Maggard, "Copper(I)-based p-type oxides for photoelectrochemical and photovoltaic solar energy conversion," *Chem. Mater.*, vol. 28, pp. 5999–6016, 2016.
- [59] Y. J. Jang and L. S. Lee, "Photoelectrochemical water splitting with p-type metal oxide semiconductor photocathodes," *ChemSusChem*, vol. 12, p. 1835, 2019.

- [60] T. Arai et al., "High-throughput screening using porous photoelectrode for visible-light-responsive semiconductors," *J. Phys. Chem. C*, vol. 111, p. 7574, 2007.
- [61] S. P. Berglund et al., "Screening of transition and post-transition metals for photoelectrochemical hydrogen evolution," *Phys. Chem. Chem. Phys.*, vol. 15, pp. 4554–4565, 2013.
- [62] A. Elaziouti et al., "Preparation and characterization of p–n heterojunction CuBi₂O₄/CeO₂," *J. King Saud Univ. Sci.*, vol. 27, pp. 120–135, 2015.
- [63] F. Wang et al., "Spray pyrolysis of CuBi₂O₄ photocathodes: Improved solution chemistry," *J. Mater. Chem. A*, vol. 5, pp. 12838–12847, 2017.
- [64] "Copper," Royal Society of Chemistry. [Online]. Available: <https://www.rsc.org/periodic-table/element/29/copper> [Accessed: Apr. 30, 2022].
- [65] "Bismuth," Royal Society of Chemistry. [Online]. Available: <https://www.rsc.org/periodic-table/element/83/bismuth> [Accessed: Apr. 30, 2022].
- [66] "Oxygen," Royal Society of Chemistry. [Online]. Available: <https://www.rsc.org/periodic-table/element/8/oxygen> [Accessed: Apr. 30, 2022].
- [67] L. Wang et al., "Hydrothermal synthesis of CuBi₂O₄/WO₃ heterostructure with enhanced photoactivity," *J. Hazard. Mater.*, vol. 381, p. 120956, 2020.
- [68] E. Abdelkader et al., "Novel CuBi₂O₄/SnO₂ p–n heterojunction with enhanced photocatalytic performance," *J. King Saud Univ. Sci.*, vol. 27, pp. 76–91, 2015.
- [69] F. Guo et al., "Fabrication of CuBi₂O₄/g-C₃N₄ p–n heterojunction," *Inorg. Chem. Front.*, vol. 4, pp. 1714–1720, 2017.
- [70] J. Lee et al., "Stabilized high-density CuBi₂O₄/NiO heterostructure thin film photocathode," *Chem. Commun.*, vol. 55, pp. 12447–12450, 2019.
- [71] J. Yin et al., "Charge redistribution at GaAs/P3HT heterointerfaces," *J. Phys. Chem. Lett.*, vol. 4, no. 19, pp. 3303–3309, 2013.
- [72] G. F. X. Strobl et al., "From extraterrestrial to terrestrial applications," in *Optical Sciences*, Berlin: Springer, 2008, pp. 7–27.
- [73] Z. I. Alferov et al., "Solar-energy converters based on p–n Al_xGa_{1–x}As–GaAs heterojunctions," *Fiz. Tekh. Poluprovodn.*, vol. 4, pp. 238–239, 1970.
- [74] X. Li et al., "Recent advances in noncontact external-field-assisted photocatalysis," *ACS Catal.*, vol. 11, no. 8, pp. 4739–4769, 2021.
- [75] "The Nobel Prize in Physics 2000," Nobelprize.org. [Online]. Available: <https://www.nobelprize.org/prizes/physics/2000/alferov/lecture> [Accessed: Apr. 30, 2022].
- [76] X. Wang et al., "Design of GaAs solar cells operating close to the Shockley–Queisser limit," *IEEE J. Photovolt.*, vol. 3, no. 2, pp. 737–744, 2013.

- [77] I. Schnitzer et al., "Ultra-high spontaneous emission quantum efficiency from AlGaAs/GaAs/AlGaAs double heterostructures," in *Proc. LEOS '92*, 2005.
- [78] M. Burgelman et al., "SCAPS manual," Version 8 May, 2000.
- [79] H. J. Pauwels and G. Vanhoutte, "Influence of interface states on heterojunction solar-cells," *J. Phys. D: Appl. Phys.*, vol. 11, pp. 649–667, 1978.
- [80] N. T. Hahn et al., "Electrochemical characterization of p-CuBi₂O₄ thin film photocathodes," *J. Phys. Chem. C*, vol. 116, no. 10, pp. 6459–6466, 2012.
- [81] A. Elaziouti et al., "CuBi₂O₄/CeO₂ photocatalytic activities under UVA light," *J. King Saud Univ. Sci.*, vol. 27, pp. 120–135, 2015.
- [82] F. Guo et al., "CuBi₂O₄/g-C₃N₄ p–n heterojunction for visible light photocatalysis," *Inorg. Chem. Front.*, vol. 4, pp. 1714–1720, 2017.
- [83] F. Wang, "Multinary metal oxides for solar water splitting," Doctoral dissertation, Tech. Univ. Berlin, Germany, 2017.
- [84] G. Sharma et al., "Electronic structure of p-CuBi₂O₄ nanocrystals," *J. Mater. Chem. A*, vol. 4, no. 8, pp. 2936–2942, 2016.
- [85] B. J. Van Zeghbroeck, "Effective density of states," 1997. [Online]. Available: <https://ecee.colorado.edu/~bart/book/ex019.htm> [Accessed: Apr. 30, 2022].
- [86] S. P. Berglund et al., "Evaluation of CuBi₂O₄ for photoelectrochemical water splitting," *Chem. Mater.*, vol. 28, no. 12, pp. 4231–4242, 2016.
- [87] M. Burgelman et al., "SCAPS Manual (version: 3.3.07)," Univ. Gent, Belgium, 2018. [Online]. Available: <http://scaps.elis.ugent.be> [Accessed: Apr. 30, 2022].
- [88] M. M. A. Moon et al., "Investigation of thin-film p-BaSi₂/n-CdS heterostructure," *Phys. Scr.*, vol. 95, p. 035506, 2020.
- [89] "Semiconductor Properties," Cleanroom BYU. [Online]. Available: <https://cleanroom.byu.edu/semiconductor-properties> [Accessed: Apr. 30, 2022].
- [90] J. L. Merz et al., "Optical properties of substitutional donors in ZnSe," *Phys. Rev. B*, vol. 6, no. 2, pp. 545–556, 1972.
- [91] M. García-Rocha et al., "Structural properties of ZnSe/GaAs interfaces," *Appl. Surf. Sci.*, vol. 112, pp. 165–170, 1997.
- [92] S. W. Lehner et al., "Defect energy levels of doped synthetic pyrite (FeS₂)," *J. Appl. Phys.*, vol. 111, no. 8, p. 083717, 2012.
- [93] A. Hosen et al., "Simulating CuBi₂O₄-based thin-film solar cell," *SN Appl. Sci.*, vol. 3, no. 5, p. 1, 2021.
- [94] J. Hossain et al., "Design of FeS₂-based dual-heterojunction thin film solar cell," *Int. J. Green Energy*, pp. 1–12, 2021.

- [95] M. Kumar et al., "Lead-free Sn-based perovskite solar cell design," *Opt. Mater.*, vol. 108, p. 110213, 2020.
- [96] J. Meier et al., *Thin Solid Films*, vol. 451–452, pp. 518–524, 2004.
- [97] J. Zhao et al., *Appl. Phys. Lett.*, vol. 73, pp. 1991–1993, 1998.
- [98] M. A. Green et al., "Solar cell efficiency tables (version 54)," *Prog. Photovolt: Res. Appl.*, vol. 27, no. 7, pp. 565–575, 2019.
- [99] B. M. Kayes et al., "27.6% conversion efficiency record for single-junction solar cells," in *Proc. IEEE Photovolt. Spec. Conf.*, 2011.
- [100] "First Solar achieves cell conversion efficiency world record," First Solar, Inc., Feb. 24, 2016.